Technische Universität München

Fakultät für Medizin

Improving Quantitative Imaging Accuracy for Dosimetry of Lutetium-177-PSMA Imaging &Therapy

Elham Karimi Ghodoosi

Vollständiger Abdruck der von der Fakultät für Medizin der Technischen Universität München zur Erlangung des akademischen Grades eines Doktors der Naturwissenschaften (Dr. rer. nat.) genehmigten Dissertation

Vorsitzende: apl. Prof. Dr. Sibylle Ziegler

Prüfende/-r der Dissertation:

1. apl. Prof. Dr. Sibylle Ziegler

2. Prof. Dr. Nassir Navab

Die Dissertation wurde am 30.12.2020 bei der Technischen Universität München eingereicht und durch die Fakultät für Medizin am 08.06.2021 angenommen.

This thesis is dedicated to my family and friends who have always supported me in this journey.

Abstract

Lutetium-177 (^{177}Lu)-PSMA I&T has been extensively investigated for prostate cancer therapy. Whole-body planar imaging, single-photon emission computed tomography/computed tomography (SPECT/CT), and positron emission tomography/computed tomography (PET/CT) are imaging techniques to provide data for calculating absorbed dose of ^{177}Lu-PSMA I&T to organs. Additionally computed tomography (CT) is used to aid absorbed dose calculation. Overlapping activity distribution is expected to affect the calculated dose based on calibrated planar images of the whole body. The aim of this work is to improve quantitative SPECT/CT imaging accuracy for the purpose of dosimetry of ^{177}Lu-PSMA I&T.

For this purpose, SPECT calibration was performed in air or water using two vials with different sizes, and different calibrated activities. Mean calibration factor (CF) using both gamma photopeak energies of ^{177}Lu for large (mCF_L) and small (mCF_S) volumes of interest (VOIs) was calculated independently. Data were acquired using a commercial SPECT/CT (SIEMENS SYMBIA T6) and reconstructed by collimator detector response (CDR) correction, attenuation correction (AC), and scatter correction (SC). For SC, triple energy window (TEW) correction was applied for both photopeak energies of ^{177}Lu.

The influence of scatter energy window widths, SC methods, and attenuation map scaling (at 113, 175, 190, and 208 keV) on the CF calculations was evaluated using SIMIND Monte Carlo simulation program. Two different SC methods, 1) effective scatter source estimation (ESSE) and 2) TEW were applied to reconstruct simulated projections. The collimator detector response and attenuation correction were implemented in both correction methods.

Using the mCF_L the deviation of calculated activity from the true activity, was larger than mCF_S. The mCF_L and mCF_S in water were 4.5±0.8 and 4.8±0.72 counts per

second MBq^{-1}, respectively. Regardless of activity concentration value, it was observed that the calculated CF for the medium vial was higher than the one calculated for the small vial.

The reference CF for the water-filled phantom considering all photons, excluding scattered events, based on simulation results was equal to 3.3 cps MBq^{-1}. Using the generated attenuation map at 190 keV, the calculated CF for 113 and 208 keV was about 10% smaller and larger than the one generated at 175 keV, respectively. The calculated CF by applying the TEW correction was 17% higher than the value calculated by the ESSE correction method for a water-filled phantom. However, our findings showed that an appropriate scatter window combination can reduce this difference between TEW and ESSE methods to 3%. The proper scatter correction was obtained by applying a wider SW for the 113 keV and a narrower SW for the 208 keV in respect to the clinical settings. Since the TEW is a commonly used technique in clinical practice, current work implies that choosing a suitable width of the scatter window (SW) may reduce under/over-estimation in dose calculation. Moreover, it is suggested to generate and apply the attenuation map at 113 and 208 keV, individually. Using the mCF_L obtained from phantom measurements, ^{177}Lu-PSMA I&T uptake in the liver and kidneys of six patients was measured. For this purpose, the patient data were collected using SPECT images, at five time points; 2, 24, 48, 72, and 168 hours post injection (p.i.). The planar whole body images were acquired at the same time points. The absorbed dose to each organ was calculated using OLINDA/EMX software and the data from planar and SPECT images were compared. In this limited patient cohort, the absorbed dose to the kidney using SPECT/CT and planar data ranged from 0.42 Gy GBq^{-1} to 0.88 Gy GBq^{-1} and from 0.39 Gy GBq^{-1} to 0.92 Gy GBq^{-1}, respectively. The average absorbed dose to the kidney based on planar images was 23% higher than the dose calculated from SPECT/CT data (0.69±0.24 Gy GBq^{-1} vs 0.53±0.21 Gy GBq^{-1}). Moreover, the absorbed dose to the liver using SPECT/CT and

planar data was about 0.074±0.019 Gy GBq^{-1} and 0.097±0.05 Gy GBq^{-1}, correspondingly. The difference in dose values based on planar or/and SPECT/CT data was less than the inter-individual variation.

Table of Contents

1 Introduction 2
1.1 Background 2
1.2 An overview of biomedical imaging 8
1.3 Principles of gamma camera imaging 11
1.4 Principle of SPECT image reconstruction 14
1.5 Image degrading factors and related reconstruction methods 17
1.6 Absorbed dose calculation 27
2 Methods 29
2.1 Phantom measurements 29
2.1.1 Acquisitions 29
2.1.2 Calibration measurements 31
2.1.3 Estimating the calibration factor by defining volume of interest (VOI) 34
2.2 Simulation using a Monte Carlo method- SIMIND 36
2.3 Patient study 47
2.3.1 Patient data 48
2.3.2 Estimation of the activity uptake using planar images 48
2.3.3 Estimation of the activity uptake using SPECT images 50
2.3.4 Patient specific organ dose calculation using OLINDA/EXM software 51
3 Results 54
3.1 Phantom measurements 54
3.2 Simulation using the SIMIND Monte Carlo code (SMIND) 59
3.3 Patient study 67
4 Discussion 72
4.1 Calibration factor calculated by the phantom measurements 72
4.2 Analyzing the simulation results 73
4.3 Analyzing the measured activities and doses from patient data 77
Conclusion and future work 80
List of abbreviation 85
List of tables 87
List of figures 88
Bibliography 91
List of publication 99
Acknowledgements 100

1 Introduction

1.1 Background

Prostate cancer (PC) is the second most commonly diagnosed cancer and the fifth leading cause of cancer death in men [1]. Although prostate cancer is diagnosed as a localized disease in most patients, there is a considerable cohort of patients with metastatic disease named as advanced prostate cancer. Targeted radionuclide therapy (TRT) has been implemented for advanced prostate cancer treatment [2]. Minimizing the radiation dose to the normal organs while giving a proper dose to the tumor is one of the most important advantages of this method.

To choose an ideal therapeutic radionuclide, the size of the lesion should be taken into account in order to transfer the desired energy into the tumor while protecting the surrounding healthy tissues. Because of its desirable physical properties (significant half-life, gamma photopeaks and electron energy), lutetium-177 (^{177}Lu) is an ideal radionuclide of choice compared to the other radionuclides utilized in TRT, Table 1.1.

Table 1.1: Common radionuclides used in targeted radiotherapy [3].

Radionuclide	Physical half–life ($T_{1/2}$) in days	Radiation Type in MeV	Particle range in mm
^{131}I	8.02	β (0.6), γ (0.364)	2
^{65}Cu	2.58	β (0.54), γ (0.185)	1.8
^{90}Y	2.67	β (2.28)	12
^{186}Re	3.77	β (1.08), γ (0.131)	5
^{177}Lu	6.73	β (0.497), γ (0.208 & 0.113)	1.5

In Table 1.1, common radionuclides used in targeted radiotherapy are reported. It is common to use ^{177}Lu in prostate cancer therapy, mainly because the emitted electrons from ^{177}Lu have short ranges in tissue, moreover they deliver all their energy in a small area. Furthermore, ^{177}Lu emits two energy gamma rays at 208 and 113 keV with 10.36

1.1 Background

and 6.17% abundance, respectively [4]. These ^{177}Lu gamma rays in the context of medical imaging can be used for collecting data from tumor and other dose-limiting organs, e.g. kidneys and liver. Later, the collected data can be used in dosimetry. In addition, the relatively long physical half-life of ^{177}Lu (6.73 days) is suitable for delivering sufficiently high radiation to the tumor.

Cancer targeting relies mainly on proper diagnostic and therapeutic markers to deliver significant dose to the target organ, hence lots of efforts have been made in this regard in the past decades. Different ^{177}Lu-labeled peptides like ^{177}Lu-RGD-BBN heterodimeric peptide, ^{177}Lu-GRP-R Agonist, ^{177}Lu-DOTATATE and ^{177}Lu-PSMA I&T are extensively investigated in literature [5-9].

The possibility of using ^{177}Lu-labeled prostate specific membrane antigen (PSMA) ligand as a sustainable imaging and therapeutic agent for patients with metastatic prostate cancer has been highlighted in recent literature [7-14].

Tracing ^{177}Lu-labeled conjugates within patient's body is crucial to calculate the absorbed doses of individual organs. For this purpose, planar whole body images are used to quantify organ absorbed activity [15-17]. Bailey et al. [16] introduced a procedure to obtain quantitative whole body planar images for the ^{177}Lu-DOTA-octreotate. They acquired planar whole-body images in four time points; one immediately after injection of ^{177}Lu-DOTA-octreotate and the others approximately 4, 24 and 96 hrs after the first scan. The authors concluded that due to superimposition of different organs and tissues in 2D images, dose estimation based on planar images is limited. A large variation of absorbed dose in a kidney was reported by Larsson and colleagues in cohort of patients [17]. They emphasized that an individual dosimetry is crucial for normal organs like kidneys for optimal treatment.

The accuracy of internal dosimetry depends on quantification of the accumulated activity over time, hence obtaining an absolute quantitation in various organs is essential. Full quantitative SPECT may improve the dose calculation in this respect.

1.1 Background

The quantitative estimation of absolute radiation dose in TRT have recently been investigated in two independent studies [15, 18].

A direct measurement of radiation dose without necessity of calibration of the dosimeter response is known as absolute dosimetry [19]. For absolute dosimetry approach in TRT, the counts per voxel need to be converted into the activity value when an image is reconstructed. To this aim, dosimetry based on quantitative SPECT imaging requires a calibration factor. This factor depends on the type of the collimators, the sensitivity of the camera for the utilized energy windows, as well as the effect of attenuation and scatter. Since ^{177}Lu has two main gamma photopeaks, the image acquisition and reconstruction parameters (e.g. photopeak scatter energy window's width, scatter correction (SC), and attenuation map for attenuation correction (AC)) need to be optimized for accurate quantitative data collection.

Some protocols based on ^{177}Lu TRT have been provided by the internal dosimetry schema of the Medical Internal Radiation Dose (MIRD) Committee of the Society of Nuclear Medicine and International Atomic Energy Agency [15, 18]. The data acquisition and reconstruction parameters are two key factors for CF estimation. For example, the choice of the photopeak energy window considering the energy spectrum of emitted photons and the estimation of attenuation map affect the activity quantification and hence the dose calculation. Dewaraja et al. [15] in MIRD pamphlet No. 23 presented an overview of requirements for 3D SPECT imaging for dosimetry. Based on Dewaraja et al. [15], it was emphasized that during phantom measurement, the experimental condition should be close to the clinical setting. Indeed, the accuracy of calibration factor, which is used to convert the total counts to the true activity strongly, depends on the accuracy of implemented attenuation and scatter correction. Moreover, Dewaraja et al. [15] reported that even by applying collimator detector response (CDR) compensation underestimation of measured activity on the voxel level for a small object relative to the SPECT at full width at half maximum (FWHM) (5-

25 mm) may occur. In MIRD pamphlet No. 26 [4] it was advised that using medium energy (ME) collimator for both gamma photopeak energies is suitable for quantitative SPECT imaging with ^{177}Lu. Moreover, in MIRD pamphlet No. 26 [4], it has been concluded that the ratio of scatter photons to the total photons for the 113 keV main window is much higher than for the 208 keV main window because of the large contribution of down-scattered 208 keV photons in the main energy window of the low gamma photopeak. Hence, it is important to use a reliable scatter correction method to compensate for the contribution of undesired scatter photons. Furthermore, some scatter correction methods such as effective scatter source estimation (ESSE) or analytic photon distribution interpolative (APDI) methods were recommended in [4]. The recommended width for main energy window, using ME collimator is 10-20% centered on the 208 keV. Moreover, for attenuation correction it was suggested to create attenuation map for each gamma photopeaks.

Recently, accuracy of CF calculation, camera sensitivity, and recovery coefficient (RC) based on several reconstruction parameters e.g. the attenuation correction, the scatter correction, and the collimator detector response compensation have been investigated [4, 14, 15, 20-31]. In 2010, Sandström et al. [25] calculated the calibration factor as the ratio of total counts in the volume of interest (VOI) to injected activity using a spherical source with 100 ml volume including 1 GBq ^{177}Lu. The VOI was defined in two different methods; a large VOI which was 20% larger than the source volume and a small VOI in the center of the source with 4 ml volume. The calculated calibration factor using the small VOI was about 1.3 times greater than the one obtained by large VOI. They concluded that using small VOIs may reduce the partial volume effect, and using planar images results in overestimation in dose calculation compared to SPECT images. Sanders et al. [21] proposed an extension of the quantitation protocol to the therapeutic use of ^{177}Lu. In their work considering both photopeak energies of ^{177}Lu (208 keV and 113 keV), the CF was calculated using a

6.2-liter cylinder and applied to define the RC of six spheres with different volumes (0.5 ml-16 ml). The width of the scatter energy window for each of the main photopeaks was in the range of 15% - 20%. The results demonstrated that the value of the CF (as a major physical factor in quantitation of ^{177}Lu) is sensitive to the choice of photopeak, and is even more sensitive when the lower photopeak energy is used. Recently D'Arienzo et al. [27] suggested that using 208 keV photopeak energy of ^{177}Lu results in sufficient accuracy for CF calculation. The results showed that the deviation of measured activity from known activity is in the range of -11.6% to 7.3%. De Nijs et al. [24] implemented two different scatter window widths for each of the gamma photopeak energies of ^{177}Lu for TEW method. The smaller window had 4 keV and the broader one had 10 keV width. They concluded that, as the TEW is noise sensitive, using wider windows is more stable for dynamic studies. In addition, they suggested that the ESSE should be applied as a standard correction technique if both gamma photopeak energy windows are used. The effect of SC method on the camera normalizing factor (CNF) using SPECT images was illustrated by Uribe et al. [28]. Considering only 208 keV photopeak energy, they applied two different SC methods; TEW and the analytical photon distribution interpolation (APDI). To evaluate the effect of object volume they used different spheres and bottles filled with ^{177}Lu in phantom measurements. They determined that in the absence of background, the TEW technique causes under or overestimation of the activity for small and large spheres, respectively. The authors for lesions in non-uniform attenuation areas recommended the APDI method. Hippeläinen et al. [26] studied the effect of several compensation methods on the concertation recovery coefficient (cRC) using the high photopeak energy of ^{177}Lu. They applied different combination of correction methods; attenuation, attenuation+collimator detector response and attenuation+collimator detector+scatter. The SC was performed using an accelerated Monte Carlo (MC) simulation method. By including CDR compensation, cRC was improved compared

with applying only the attenuation correction. They found that their method for SC improves the accuracy of cRC, especially for small sources.

Along the experimental measurements, MC based simulation technique is one of the standard methods to verify image degrading factors, to validate quantitative SPECT/CT imaging, and to estimate 3D distribution of activity in different organs [32-35]. The ability to investigate the effect of different parameters during image acquisition and reconstruction is the main advantage of simulation methods. Nevertheless, different physical factors such as collimator detector response (CDR), attenuation and scatter compensation can be simulated and their effects in the reconstruction algorithm can be studied [36, 37]. Among the various simulation tools, SIMIND as a MC based code, is commonly used for standard clinical SPECT camera [38].

Besides the simulation and phantom studies, the impact of image quality and image registration on the image-based dosimetry has been investigated in literature [18, 39-41].

As reported in [17], anatomical images are suggested to be used to obtain a sufficient density map for MC-based dosimetry. They reported that CT images can be used to identify anatomical information of the patient body and to create an appropriate attenuation map for AC. Li et al. [41] studied the accuracy of image segmentation for delignating the region of target organs. They concluded that improving image quality and quantitation lead to a more accurate activity estimation in TRT.

To improve the image quality, an accurate alignment of SPECT and CT images is required for a valid SPECT/CT image. In clinical practice, this procedure is carried out using an image analyzing and registering software. In the case of misregistration, a manual alignment is needed. Besides the SPECT/CT imaging, a series of diagnostic scans are also acquired using positron emission tomography (PET)/CT. The quality of CT images obtained from PET/CT, as a specific diagnostic CT, are higher than the

ones obtained from SPECT/CT. Hence, suitable registration between these two series of CT images, improves the image quality for the purpose of target area delineation. Many studies have been performed on co-registration between CT and MR images [42-46].

In general, quantifying ^{177}Lu-PSMA I&T activity in individual organs using 3D quantitative SPECT images is more complicated than quantifying activity in whole body planar images at multiple time points. It is questioned whether a simplified imaging protocol, not requiring a full-body SPECT scan, can yield sufficiently reliable dosimetry data. Moreover, dosimetry based on quantitative SPECT imaging requires a calibration factor to convert the obtained counts from the images to the activity. This factor is very much depended on the collimator type, the sensitivity of the camera after the utilized energy windows, defining the VOI, and the effect of attenuation and scatter.

In this work, by performing both phantom and simulation measurements, we investigated the influence of the SW width, photopeak energy window, activity distribution, object size, attenuation map, SC and VOI definition on quantitative SPECT of ^{177}Lu-PSMA I&T data. In addition, an individual dosimetry has been performed for six patients using SPECT and planar images separately and the results have been compared.

In the following sections an overview of nuclear imaging, a number of image degrading factors and related compensation methods will be described.

1.2 An overview of biomedical imaging

Imaging technique for the analysis of diseased organs and tissues within the body is known as biomedical imaging. Today's imaging tools enable us to observe biological processes more clearly than ever before. A biomedical imaging study can provide insight into biological processes such as the kinetics of receptors, cellular signaling,

interactions, and molecule movement across membranes. In addition to being mostly noninvasive, biomedical imaging offers precise tracking of metabolites that can be used to identify disease, track progress, and monitor response to treatment [47].

Recent progress in multimodal imaging techniques such as digital radiography, CT, SPECT, and PET enhanced the robustness and accuracy of clinical diagnosis. Alignment of functional and structural images, mapping the functional information into anatomical space, significantly improved our knowledge about mechanisms involved in diseases. It resulted in development of more advanced therapeutic protocols, and approaches for the analysis of intact 3-dimensional bodies.

In the following subsections, the well-known imaging systems being used in this work, are listed and explained briefly.

1.2.1 CT imaging (an anatomical imaging modality)

CT is one of the most common anatomical imaging modalities. In this imaging system, the X-ray beam is used to collect information about the tissue, but the image is not a normal projection view. This image is a cross-sectional view of the X-ray attenuation of different tissues in the patient's body. Typical computed tomography produces cross-axis images oriented along the anatomical plane of the lateral dimension of the anatomical structure. A series of X-ray images recorded from different angles around an object are combined and then reconstructed by a computer-applied algorithm. These images consist of pixels, which each pixel has certain dimension. The pixels correspond to certain depths; volume pixels are called voxels. In other words, the pixel or voxel value represents the attenuation intensity of the X-ray beam by the tissue compared to the attenuation of the same X-ray beam by water. Differences in attenuation between neighboring organs results in X-ray imaging contrast. However, differentiating between two adjacent pixels or voxels is a challenging task, especially

at the interface of tissues. This phenomenon, known as partial volume effect, causes many pixels to include one or more tissue elements [48]. Thus, alternative strategies for partial-volume compensation are of great interest.

In practice, raw CT pixels are scaled into Hounsfield units (HUs) to correspond to different tissue values. HUs represent relative quantitative measures of radiodensity used by radiologists in interpreting computed tomography (CT) images. When CT images are reconstructed, the attenuation/absorption coefficient of radiation within a tissue is taken into consideration. HUs are calculated by linearly transforming the baseline linear attenuation coefficient of the x-ray beam, where this value for distilled water (at a standard temperature and pressure) and air is equal to 0 and -1000, respectively [48, 49]. Equation 1.1 shows how to calculate HU for other tissue[48]:

$$HU = 1000 \times \frac{\mu - \mu_{water}}{\mu_{water} - \mu_{air}}, \quad (1.1)$$

where, μ is original linear attenuation coefficient of substance, μ_{water} is linear attenuation coefficient of water, and μ_{air} is linear attenuation of air.

Chapter 2.2 includes more details of using HU in calculating attenuation coefficient.

1.2.2 Nuclear imaging

As explained before, an in vivo functional imaging of organs can be obtained by using a suitable radiolabeled nuclide (radiopharmaceutical). The gamma probes are the first generation of gamma detecting devices, which were used to detect the administrated radioactivity as well as to quantify the amount of radioactivity in the whole body [50-52]. Following gamma probes, the planar imaging system was the first nuclear imaging modality providing 2D images (planar images). In 1950, Benedict Cassen manufactured the first automated scanning system that was comprised of a motor driven scintillation detector coupled to a relay printer. The rectilinear scanner was used to image thyroid glands after the administration of radioiodine [53]. The planar

imaging method is still a common imaging method used in clinical practice for functional imaging of different organs.

Based on the property of the administrated radiopharmaceuticals and the number of gamma detectors, the emission tomography divides into two modalities: 1) PET and 2) SPECT. In PET, which includes multiple rings of gamma detectors, a positron emitting radionuclide-labeled tracer is used. Therefore, the PET imaging is based on detection of paired annihilation photons, which emitted in opposite directions after recombination of a positron with an electron within the patient's body. The position of recombination coincidence can be located on a line of response after the detection of both emitted gamma photons. Finally, by using a large number of measured lines of responses a 3D distribution of the radioactivity is reconstructed. In contrast, in SPECT system which has one or two gamma detectors, the administrated radionuclides are gamma or beta-gamma emitters. In this imaging modality, the images are acquired at different angles of rotation of the gamma detector.

1.3 Principles of gamma camera imaging

In nuclear medicine, the emission of a gamma ray is a very small-scale nuclear phenomenon. A gamma camera is designed in such a way to translate this radiation into an electrical signal in order to be detected and measured. A map of a radioactive nuclei distribution is created by readings these electric signals. This map provides the necessary information in diagnostic and therapeutic purposes. Hal Oscar Anger proposed the first design of a gamma camera. Hence, it is often referred as "Anger Camera" [54]. In general, as shown in Figure 1. 1, a gamma camera head consists of:

1. Collimator
2. Scintillating crystal
3. An array of photomultiplier tubes
4. Anger logic circuit

1.3 Principles of gamma camera imaging

The collimator is made of a thick plate of lead or tungsten punctured with a number of very thin parallel channels. At the center of a gamma camera, a large rectangular crystal often made of sodium iodide and doped with thallium, NaI (Tl), is placed. The role of this crystal as a detection element is to stop the gamma rays and convert portion of the deposited energy into scintillation. Only the gamma rays with normal direction to the surface of the collimator plate and crystal can pass through the collimator. An array of small photomultipliers (PMTs) is located behind the crystal, which converts photons into electric signals. Among the various hits in a set of photomultipliers, one can determine the energy of the hitting gammas, and approximate the position of their impact on the crystal. By using "Anger logic" circuit, it is possible to calculate the centroid of the signals from each PMT by knowing its relative position [55]. If the energy of the gamma ray is not in the range of the energy of the radioactive sample, it will be discarded. However, due to the limited energy resolution of scintillation detectors, a large fraction of primary photons will also be rejected by using small energy window width, resulting in clinically unacceptable examination time. Therefore, the width of the energy window must be chosen wide enough to increase sensitivity (the detection rate of the primary photons) and to reduce the examination time [56].

1.3.1 Quantitative planar imaging

A planar image is a 2D projection of radioactivity distribution within the organs. It means that only the emitted photons in a certain direction contribute in the final image. Hence, this image gives no information about the activity distribution in the depth dimension, complicating determination of the contribution of the total signal from different overlapping structures[18]. This results in poor image contrast and low accuracy in quantitative analysis. For instance, the liver and right kidney could overlap

in the posterior-anterior position, making it difficult to distinguish counts originating from each of these organs in the frontal planar projection image.

Depending on the type of acquisition (single planar image or whole body scanning), calibration factors need to be measured for corresponding acquisition protocols. It is also advantageous to acquire an image before voiding in order to compare measured total body activity versus administered activity.[18].

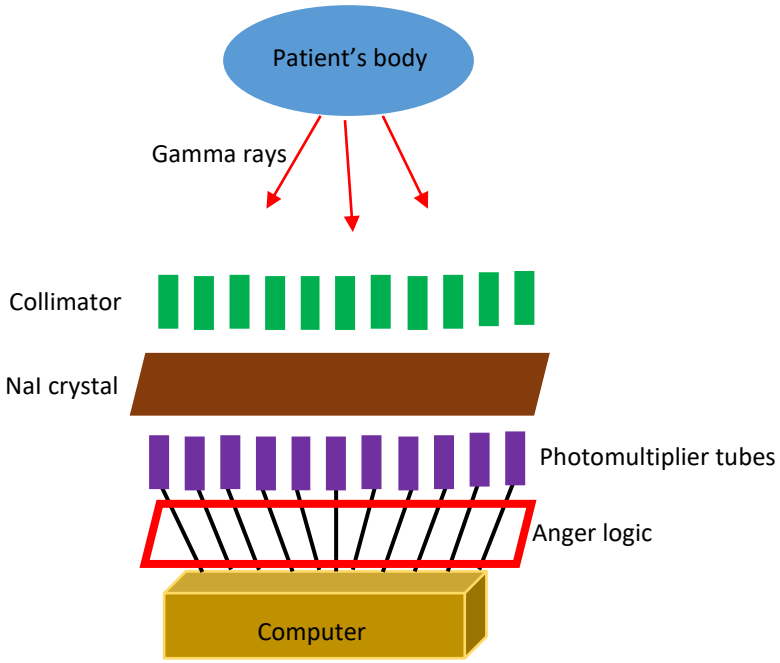

Figure 1. 1: Schematic of scintillation camera performance.

1.3.2 Quantitative SPECT imaging

The limitations of planar imaging in the determination of the activity distribution in 3D can be resolved by SPECT imaging technique. In SPECT imaging, the gamma camera rotates around the patient and acquires a large set of planar projection images at different angles, which provide projection views of the radioactivity distribution.

Since the photons are attenuated within the source (i.e., the human body) before being detected by the camera system, there is a significant decrease in detected activity [57]. The main cause of attenuation throughout the diagnostic energy range is Compton scattering, which results in changing photon directions and losing energy. Hence, changes in direction of a photon prevents it from being detected and cause a missed count. Moreover, the scattered photon can often be detected (in a wrong location) causing a false background. It is possible to compensate these deficiencies by utilizing appropriate correction methods and incorporating the techniques of CT in the image acquisition.

1.4 Principle of SPECT image reconstruction

The goal of the SPECT imaging is to determine the 3D distribution of an administrated radiopharmaceutical within the patient's organs accurately. For this reason, reconstruction of the acquired image is crucial. Assuming that photons pass through the patient's body with no attenuation, and then photons are scattered and detected by a collimator with ideal spatial resolution. For 2D distribution the SPECT image reconstruction estimates the distribution of a radiopharmaceutical in body tissue, *f(x,y)*, from the detected photons. Based on [58] the exponential Radon transform represents the modified projection as

$$R(\theta, s) = \int_{-\infty}^{+\infty} f(s(cos\theta, sin\theta) + t(-sin\theta, cos\theta))\, e^{-\mu(L_{\theta,s}-t)} dt, \qquad (1.2)$$

where, $R(\theta, s)$ is exponential Radon transform of image *f(x,y)*, s is the position, the function μ describes the way photons are attenuated along the measurement lines defined by s and θ, $L_{\theta,s}$ is the distance between the point B on the boundary of the uniform attenuator and the s-axis, and θ is the angle of the projection (Figure 1.2). To find the best possible estimate of the activity distribution, iterative reconstruction methods are designed based on the measured projections. This is achieved by setting a criterion that measures the quality of the estimate and designing an algorithm that

finds an optimal solution by a series of repetitive calculations or iterations. Numerous different reconstruction methods have been developed and discussed in literature [35, 58, 59].

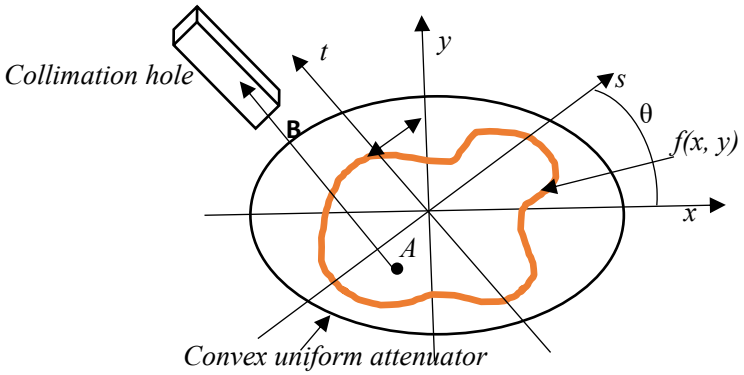

Figure 1.2: Illustration of projection coordinates corresponding to a parallel-beam scanning geometry for SPECT according to [58]: f(x,y) is radionuclide distribution, and θ is the angle of the projection.

The most common and known algorithms are 1) conjugate gradient (CG), 2) maximum likelihood expectation maximization (MLEM), 3) ordered-subsets expectation maximization (OSEM), and 4) maximum a posteriori (MAP) algorithms [60].
OSEM algorithms, introduced in 1994 by Hudson et al [36], is one of the algorithm that is widely used for both clinical and simulation purposes. This algorithm is a modification of the MLEM and requires subsets of the input data for each image to perform image reconstruction. This method improves the quality of the final image, however specific number of subsets for optimizing image quality is not known a priori. The updated formula based on the MLEM algorithm can be rewritten as following for the OS-EM method [59]:

$$x_i^{k+1} = x_i^k / (\sum_{j=1}^{J} a_{ij}) \times (\sum_{j=1}^{J} a_{ij} y_j) / \sum_{i=1}^{I} x_i a_{ij}), \quad (1.3)$$

where, x_i is the updated value of the i^{th} voxel of the image after the k^{th} iteration, y_j is the acquired projection measurement in projection bin j, and a_{ij} the probability that an event generated in voxel i is registered in projection bin j.

The difference between MLEM and OSEM methods in reconstruction simply is shown in Figure 1.3. The OSEM algorithm uses subsets in each iterations. At each updating time, a subset of the projection data is used. (Figure 1.3).

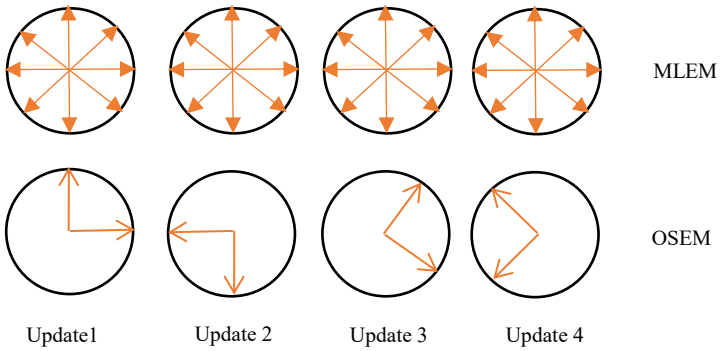

Figure 1.3: Reconstruction procedure using MLEM and OSEM methods.

To divide the projection space into a subset, various approaches are used. The common way is dividing the projection into sets with different views or angles as is shown in Figure 1.4. As reported in [61] (shown in Figure 1.4) the number of subsets and iterations severely influence the quality of final image.

The OSEM algorithm can easily vary from one system to another, as it depends on defining subset method and optimization process. Since in clinical practice, it is not possible to investigate the influence of different parameters on the image quality independently, using simulation techniques can play a crucial role in investigating the effect of each factor individually and tracking each factor's behavior during the image reconstruction procedure.

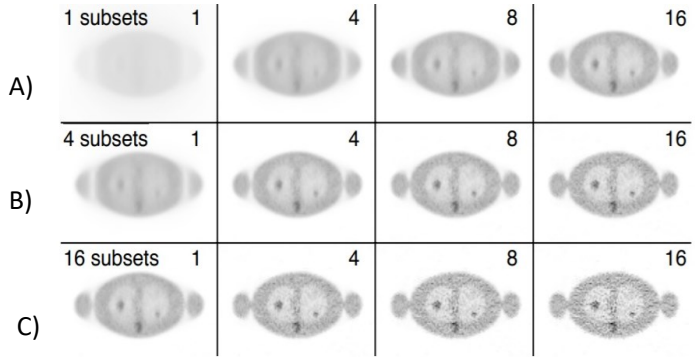

Figure 1.4: Relation between number of subsets and iterations and their effects on the quality of final image. Each row shows the number of iteration, while each column presents the number of subsets. A) 1 subset B) 4 subsets and C) 16 subsets, according to [61].

1.5 Image degrading factors and related reconstruction methods

Theoretically, in the absence of image compensation factors, an ideal SPECT image describes the total activity uptake along a line of view within a patient's body (Figure 1.5). However, in reality, several factors result in degradation in the final image and are included in reconstruction algorithms. To eliminate or reduce the effect of these factors, an appropriate correction is essential. In this section, the parameters that were investigated in this work will be explained briefly.

1.5.1 Photon attenuation

One of the major degradation factors in quantitative imaging is photon attenuation. The principle of attenuation is losing energy by a photon by transferring through a medium. The attenuation within a matter depends on the photon energy and medium density. The magnitude of this effect is greater for photons with lower energy in a denser and larger region. Also, the environmental behavior of photon transition is strongly influenced by its energy spectrum. Pure photon intensity is attenuated exponentially in a uniform medium as [62]

1.5 Image degrading factors and related reconstruction methods

$$I(x) = I_0 e^{-\mu x}, \tag{1.4}$$

where, I_0 is the primary intensity of the photon, μ the linear attenuation coefficient of a medium, x the pathway traveled by the photon in the medium, and $I(x)$ the intensity of the photon after losing its energy.

Since photon beams are made up of a spectrum of energies, the attenuation will not be exponential. Photons with lower energies are attenuated more rapidly than photons with higher energies. Therefore, the mean energy of the beam increases with attenuation, which is known as beam hardening. Low energy photons are frequently undesirable because of their contribution in scatter or surface dose; therefore, hardening correction is useful in imaging. It can be performed by adding a filter to the device that attenuates a significant portion of low-energy photons.

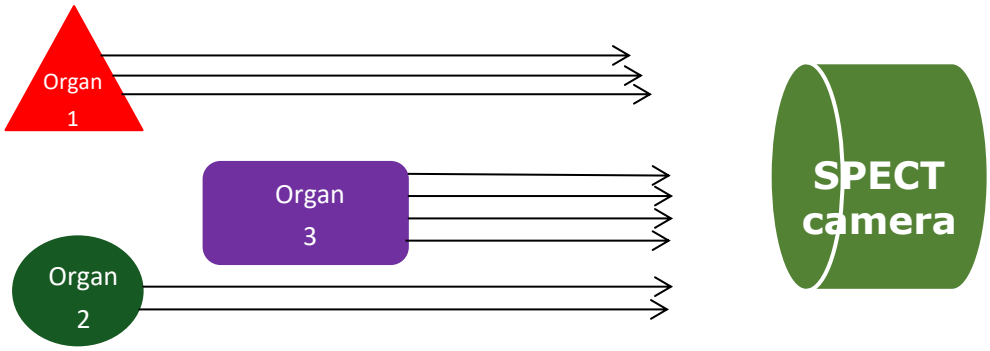

Figure 1.5: True activity measurement is possible from an ideal SPECT imaging. The emitted photons from each organ reach the SPECT camera without any attenuation and scattering.

In SPECT image reconstruction, attenuation correction affects the image's quantitative accuracy. For 2D projections, the radon transform is

$$R(r,\theta) = K \int_{-\infty}^{+\infty} f(x,y) \exp[\int_{(x,y)}^{+\infty} a(u,v)\mathrm{d}\acute{s}\,]\, ds, \tag{1.5}$$

where, $a(u,v)$ is the attenuation coefficient distribution in 2D and $\int_{(x,y)}^{+\infty} a(u,v)\mathrm{d}\acute{s}$ is the attenuation factor for photons that originate from the position (x,y) and travel inside the medium in the perpendicular direction to the detector array.

Consequently, for a non-uniform medium, estimating the attenuation is complex, and various analytical compensation methods are used for attenuation correction. The analytical methods consist of two sub-methods, exact and approximated methods [63, 64]. The exact analytical methods do not have commercial usage and their principle advantage is the short reconstruction times. In contrast, the approximated methods are used commercially. They could also be applied for the uniform attenuation distribution in desired regions. A known exact analytical method is Chang (also called zero Order Chang) compensation correction method [18]. It is utilized for a uniform medium by performing voxel by voxel attenuation compensation of an image reconstructed without attenuation compensation. To apply this method in reconstruction, the distance from the source to the surface of the object in each voxel and projection direction is computed (Figure 1.6), and then average attenuation coefficient for each voxel is calculated as

$$\overline{f_i} = \frac{1}{N}\sum_j e^{-\mu d_{ij}} , \tag{1.6}$$

where, N is the number of the projections in a voxel, μ is the attenuation coefficient of the medium, and d_{ij} is the distance of the ith voxel from the surface of the object in the direction of the jth projection.

In general, attenuation compensation methods use an attenuation map to give the attenuation coefficient that corresponds to each pixel of an image. The attenuation map can be estimated using either radiation data or transmission measurements independently.

One of the common ways to estimate the attenuation map is fitting an ellipse to the borders of the object in the emission projection data. A well-known way to measure attenuation map is using a registered CT image [65]. Considering the difference between the energy of the CT X rays and gamma emitted radionuclide, scaling the map

is necessary. If the radionuclide has more than one gamma photopeak in its decay spectrum (e.g. ^{177}Lu), the projection data is obtained by applying all main photopeaks. Hence, after generating the attenuation map, an accurate translation is required to incorporate the map into the projection data to compensate part of error caused by photon attenuation. In clinical routine, to apply the attenuation map in the reconstruction algorithm, registr8ation should be performed using the image obtained from radionuclide distribution (distributes radionuclide) in organs. As patient position during the imaging differs from one scanner to another one, it is difficult to register a CT image from an independent diagnostic scanner to the SPECT image. Hence, in clinical practice, SPECT/CT scanners are used to create the attenuation map. However, the quality of CT images of these scanners is not as good as the diagnostic CT images like CT of PET/CT. Even using SPECT/CT can cause image degradation due to miss-calibration or patient movement between the CT and SPECT acquisitions.

Attenuation map can also be measured using a radionuclide source [66, 67]. This method is used commercially but results in a noisy attenuation map with poor quality and resolution in providing proper anatomical information. If the resolution of created map fits to the SPECT image, the poor resolution does not have a considerable effect on the attenuation compensation [39].

1.5 Image degrading factors and related reconstruction methods

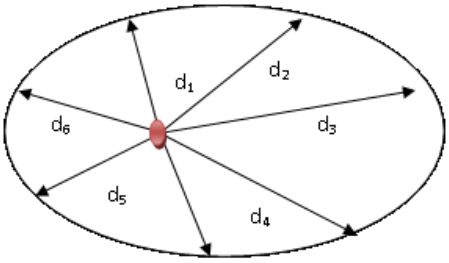

Figure 1.6: Distances from the point to the edge of the object are calculated in the Chang compensation method, according to [18].

1.5.2 Photon scattering

In SPECT imaging, the most scatter happens in the abdomen and thorax (about 40%) [68]. Similar to the attenuation, the scattering phenomenon results in quantitative errors. Photons which are scattered in small angles have a chance to be detected within the photopeak energy window. These photons carry incorrect information about the exact position where they were emitted from, consequently this can lead to inaccurate activity contrast. The contribution of scattering incident during imaging depends on various factors such as photon energy, energy window setting, source distribution, and medium which photons travel through. In the absence of the scatter photons, by using a suitable attenuation map, attenuation compensation recovers activity concentration in the organ. If the scattered photons are included in the projection data, they cause an overestimation of activity after reconstruction. Scattering happens more in the ticker and denser parts of the patient's body than the other parts. Different methods can be applied to compensate for the scatter effect in SPECT/CT images, some of these methods will be explained in the following sections.

1.5.2.1 Effective attenuation coefficient

To compensate for the scatter counts from the image projections, one of the simplest ways is using an effective attenuation coefficient to reduce the magnitude of the attenuation correction. The contrast of the images does not improve using this method,

as it does not remove the scattered photons from the reconstructed image significantly [69]. Also, this correction strongly depends on the source distribution and the medium which photons travel through.

1.5.2.2 Scatter correction based on energy window

This method is based on defining one or more additional scatter windows. The scatter component in the photopeak window (main energy window) is estimated based on measurements in one or more scatter windows which are placed in the scatter region of the energy spectrum. Dual energy window (DEW), triple energy window (TEW), and effective source scatter estimation (ESSE) are the three known scatter correction methods. These methods are briefly explained in the following subsections.

1.5.2.2.1 Dual energy window (DEW method)

In the DEW technique [70], the number of scattered photons is estimated only within a subordinate energy window in the Compton region of the energy spectrum (Figure 1.7). The width of the scatter energy window depends on the photopeak energy of the administered radionuclide. The primary counts in the main energy window are calculated by excluding the contribution of the scattered photons using the following analytical calculation:

$$C_{primary} = C_{total} - C_s \tag{1.7}$$

where, $C_{primary}$ is the detected photons excluding the scatter photons, C_{total} the total counts within photopeak energy window, and C_s is the scattered components of the photopeak window which is obtained as

$$C_s = kC_{sw}\,, \tag{1.8}$$

where, C_{sw} is number of detected scatter photons within the scatter window. The value of the k, which is known as the scatter multiplier, is calculated in two different ways: subtracted projection mode, and subtracted tomogram mode.

The subtracted projection model is based on projection data and subtracted tomogram mode is based on reconstructed data. Since the factor *k* is phantom related, hence it is calculated for each phantom study individually.

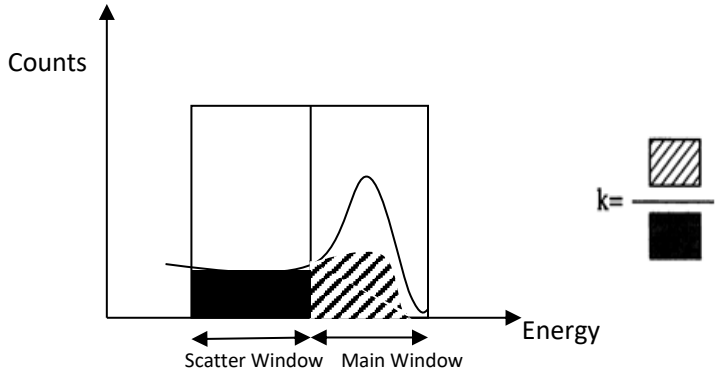

Figure 1.7: Principle of Dual Energy Window (DEW) correction for a given pixel and projection, according to [70].

1.5.2.2.2 Triple energy window (TEW) method

TEW is an energy window-based method. The main difference between TEW and DEW is the number of scatter energy windows. In the TEW method [18, 37, 71], the number of scattered photons is estimated by defining two adjacent energy windows with no overlapping on each side of the main photopeak window, which are named lower and upper scatter energy windows (LSW and USW) (Figure 1.8).

The counts of primary photons are calculated as

$$C_{Primary} = C_{total} - 0.5 \times \left(\frac{C_{lSw}}{W_{lLSW}} + \frac{C_{USW}}{W_{USW}}\right), \quad (1.9)$$

where, $C_{Primary}$ is the total counts of the primary photons in the main energy window, C_{lSw} and C_{USW} refer to the counts in the lower and upper scatter energy windows, respectively. The W_{LSW} and W_{USW} are the respective widths of the corresponding

scatter energy windows. For the photons with energies higher than photopeak, USW delineates down-scattered photons.

As the photopeak energy spectrum of an administrated radionuclide changes non-linearly in the main energy window, the trapezoidal estimation will not be perfect. Also in the case of a radionuclide with multiple photopeaks, choosing a suitable scatter energy window and optimal filtering becomes more crucial.

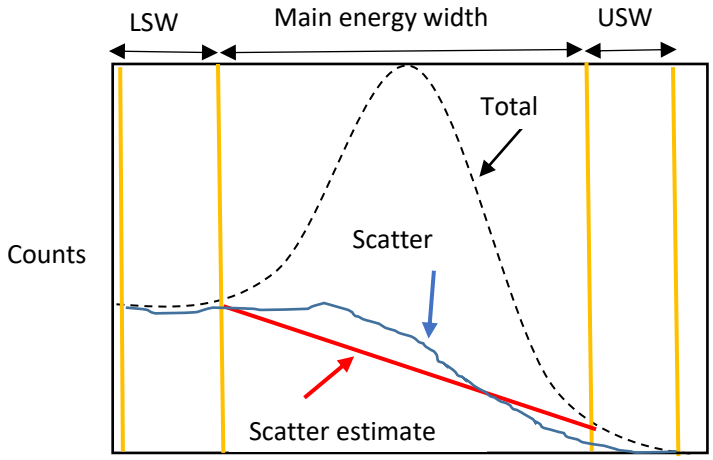

Figure 1.8: Principle of TEW scatter correction method for a given pixel and projection, according to [17].

1.5.2.2.3 Effective source scatter estimation (ESSE) method

The ESSE method is a scatter model based on using a set of scatter kernels. Two scatter kernels (k and μ_s) are required for ESSE scatter modeling. These are calculated by using a MC simulation method of a point source with a given energy spectrum in the center of a water slab [72].

Briefly, k values are the probability that a photon emitted at the center of the kernel will have its last scatter event inside the voxel of interest and be detected, excluding the probability of attenuation along the path from the voxel of interest to the detector. By convention, it resembles the probability of detecting a photon in the air. The kernel

μ_s represents the weighted average attenuation coefficient in water after the last scatter event for all photons whose last scatter event occurs in the corresponding voxel. The weighting is a detection probability for a given photon. To use these kernels in the ESSE scatter model, it is necessary to normalize the kernel image per emitted photon. In addition, the average attenuation factor image should be converted to an average attenuation coefficient image.

1.5.3 Collimator detector response (CDR)

One of the primary factors affecting the image resolution is CDR. In principle, CDR is an image which is generated from a point source of activity. It depends on the distance between the source and the collimator. The CDR has four primary components (Figure 1.9) [35]:

- The Intrinsic Response Function (IRF)
- The Geometric Response Function (GRF)
- The Septal Penetration Response Function (SPRF)
- The Septal Scatter Response Function (SSRF)

The first factor is the result of uncertainty in estimating the origin of the detected photon in the detector system and the other three depend on the collimator characteristics. The mentioned factors will be briefly explained in the following.

1.5.3.1 Intrinsic response function (IRF)

The reaction of the SPECT to a pencil beam of radiation excluding the collimator is named IRF. This function is determined by two factors: the uncertainty of position estimation in the SPECT detector and the scatter effects in the crystal. However, the scatter effects are almost negligible for low energy photons and become considerable for incident photons with medium or high energy.

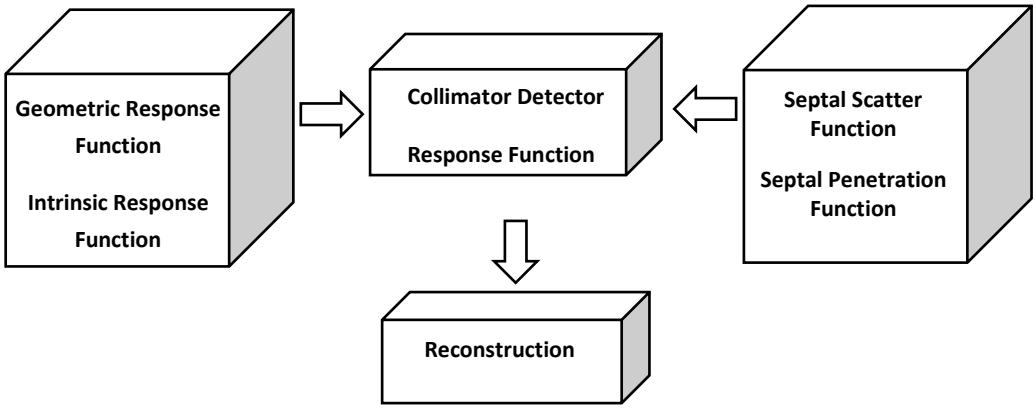

Figure 1.9: Schematic of the factors which include in collimator detector response function.

1.5.3.2 The geometric response function (GRF)

The geometric response function (GRF) represents the distribution of detected photons that travel through the collimator holes without interacting with or passing through the collimator septa.

1.5.3.3 The septal penetration response function (SPRF)

This function represents the contribution of the detected photons that penetrate through the collimator septa. Although there is no certain methodical behavior of the SPRF for multi-hole collimator, it can be studied using a Monte Carlo simulation or a beam tracer [35].

1.5.3.4 The septal scatter response function (SSRF)

The septal scatter response function describes the photons which are detected in desired energy windows after scattering in the collimator septa. In contrast to the GRF, scattering and penetration can increase total response function (TRF) width [35]. The effects of SSRF and SPRF are most important for isotopes emitting medium and high energy photons.

There are several methods to compensate for the CDR effect on SPECT images. But generally, CDR is modeled based on two separate assumptions: (1) spatially invariant,

and (2) distance dependent [35]. In this work, we did the modeling based on the second method.

1.6 Absorbed dose calculation

The energy of radionuclide absorbed by organ per unit mass is known as organ absorbed dose, which is the fundamental quantity of radiation dosimetry. Depending on the image resolution, it is possible to calculate the absorbed dose in voxel level by assuming a uniform distribution of activity within organs, the internal dose assessment is calculated based on following equation [73]:

$$D=AS, \tag{1.10}$$

and

$$S = k \sum_i n_i E_i \varphi_i m, \tag{1.11}$$

where, D is the absorbed dose in Gy, A is the activity in organ in MBq, n is the number of radiations with energy E emitted per nuclear transition, E is the energy per radiation (MeV), φ is the fraction of energy absorbed in the target, m is the mass of target region in gram or kilogram, and k is the constant coefficient.

The total absorbed dose to an organ is calculated by integration of absorbed dose rate over time. In some cases, dose rate can explain the biological effect of a radiopharmaceutical on specific organs. In equation 1.10, only A is time dependent, hence the equation can be rewritten as

$$\int_0^\infty D\, dt = \frac{k \sum_i n_i E_i \phi_i}{m} \times \tilde{A}, \tag{1.12}$$

where, $\tilde{A}$ is accumulated activity defined as:

$$\tilde{A} = \int_0^\infty A(t)\, dt, \tag{1.13}$$

1.6 Absorbed dose calculation

To facilitate absorbed dose calculation, Radiation Dose Assessment Resource (RADAR) "Task Group" of the Society of Nuclear Medicine proposed following expression:

$$D_T = \sum_S N_s \times DF(T \leftarrow S), \tag{1.14}$$

where D_T is the absorbed dose in target organ, N_s is the number of nuclear transitions that occur in the source organ, and DF is the 'dose factor' for source region S irradiating target region T.

With the improving reconstruction techniques, SPECT image will present the more precise spatial and temporal data on three-dimension for internal dosimetry scheme, which is evolving from population- and organ-average to patient-specific dose estimation [74]. SPECT voxel values are typically expressed in number of counts (cts), and the quantification goal is to determine the calibration factor CF to convert cts to Bq. According to the MIRD recommendations for the quantification [4], the CF is computed using a SPECT acquisition of a large source of a known activity in a determined phantom. Typically, a water phantom with a similar activity concentration used in clinical practice, and is imaged with the exact same parameters as in the clinical study where the calibration factor will be used. SPECT images should be reconstructed with a method that includes attenuation correction (AC) based on CT, scatter correction (SC) based on double- or triple energy window (DEW or TEW) methods , and collimator-detector response (CDR) compensation [75].

2 Methods

Part of this chapter has been published in following publications:

- Karimi Ghodoosi, E., D' Alessandria, C., Li, Y., Bartel, A., Köhner, M., Höllriegl,V., Navab, N., Eiber, M., Li, W.B., Frey, E., Ziegler, S. (2018): The effect of attenuation map, scatter energy window width, and volume of interest on the calibration factor calculation in quantitative ^{177}Lu SPECT imaging: Simulation and phantom study. Physica Medica 56, 74-80
- Karimi Ghodoosi, E., D'Alessandria, C., Eiber, M., Li, W.B., Navab, N., Ziegler, S.: Comparison of absorbed dose to kidneys using quantitative SPECT/CT and whole body planar images for Lu-177-PSMA I&T in prostate cancer therapy. Eur. J. Nucl. Med. Mol. Imaging 45, S112-S113 (2018)

2.1 Phantom measurements

For quantitative SPECT, a calibration scan is required to rescale measured counts per second (cps) and calibrated activity in the field of view (FOV). Hence, in this work phantom measurements were performed with different geometries.

2.1.1 Acquisitions

All acquisitions were performed on a SIEMENS SPECT/CT (SYMBIA T6) in the Nuclear Medicine Department of Klinikum Rechts der Isar (Munich, Germany) with a medium-energy low-penetration collimator (MELP). The main parameters of the clinical settings utilized for the acquisition are presented in Table 2.1. The image acquisition duration took 15 minutes by creating 90 projections covering 360˚ angles. The images were reconstructed by an ordered subset expectation maximization (OSEM) algorithm [36] implemented by the vendor (Siemens Health Flash 3D) and CDR compensation was included in the OSEM algorithm [76]. The compensation for

2.1.1 Acquisitions

image-degrading factors was performed by scatter correction, and attenuation correction based on CT data. The number of iterations and subsets were set as 15 and 8, respectively. For scatter correction, the triple energy window (TEW) correction method [37] was applied by considering the two main gamma photopeak energy windows of ^{177}Lu: 113 and 208 keV. To create the attenuation map, there was no possibility to choose the ^{177}Lu gamma energies; therefore, it was created for 190 keV photons (krypton-181 gamma photopeak energy). The collimator detector response compensation was automatically performed. All used SPECT reconstruction parameters are reported in Table 2.2.

Table 2. 1: SPECT acquisition parameters (clinical setting).

Acquisition	
Collimator	Medium-energy low-penetration (MELP)
Matrix	128×128
Scan arc (˚)	180
Number of projections	90
Pixel size (mm^2)	4.8×4.8
Dwell time (sec)	10
Photopeak main energy windows:	
Photopeak 1: 113 keV	113 keV±10% width
Photopeak 2: 208 keV	208 keV±6% width
Scatter energy windows:	
Photopeak 1: 113 keV	92.4 keV±10% width (LSW)[a] 131.6 keV±6.5% width (USW)[b]
Photopeak 2: 208 keV	183.6 keV±6.2% width (LSW) 230.8 keV±4.5% width (USW)
(LSW)[a]: lower scatter window; (USW)[b]: upper scatter window	

2.1.2 Calibration measurements

Table 2.2: SPECT reconstruction parameters (clinical settings).

Reconstruction	
Method	Flash 3D (Siemens)
Corrections	Attenuation, scatter (TEW), and collimator detector response
Iteration (i)/Subsets(ss)	15i/8ss
Transverse reconstructed matrix	128×128
Filter post reconstruction	Gaussian 12 mm

LSW)[a]: lower scatter window; (USW)[b]: upper scatter window

2.1.2 Calibration measurements

In this work, a National Electrical Manufacturers Association (NEMA) IEC body phantom (Model PET/IEC-BODY/P) [77] was used with 9.7 liter capacity as a body. Two different vials, one of a medium volume (180 ml) and one small volume (25 ml), were inserted to represent a kidney and a lesion, respectively (Figure 2.1). The vial with medium volume was an oval shaped bottle with 8 cm height and 0.04 cm thickness, and the small one was a cylinder bottle with 5 cm height and 3.2 cm diameter. This specific volume of 180 ml in phantom measurements was chosen because the average volume of a kidney measured from six patient CT data sets was 180±26.5 ml (Figure 2.2).

The phantom was either filled with water or air, and the small or the medium vial was fixed to the bottom of the phantom. To study the influence of the activity concentration of the source vials on the CF, the calibration process was repeated seven times with different activities of ^{177}Lu (Table 2.3).

2.1.2 Calibration measurements

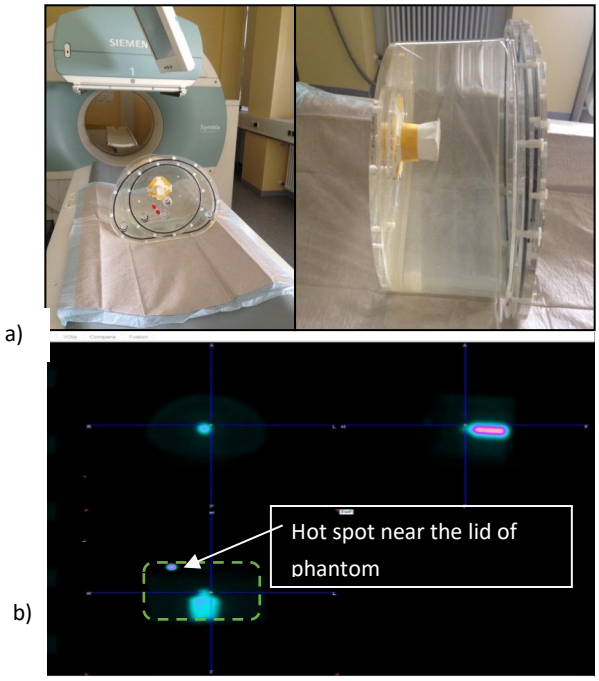

Figure 2.1: a) Siemens Symbia T6 SPECT/CT with NEMA IEC body phantom filled with water including a vial with 25 ml volume (calibrated activity of 651 MBq). b) Anterior SPECT image of water filled phantom (green) with background activity of 178.1 MBq including a 180 ml vial with 440 MBq activity. Background activity distribution was non-uniform (hot spot).

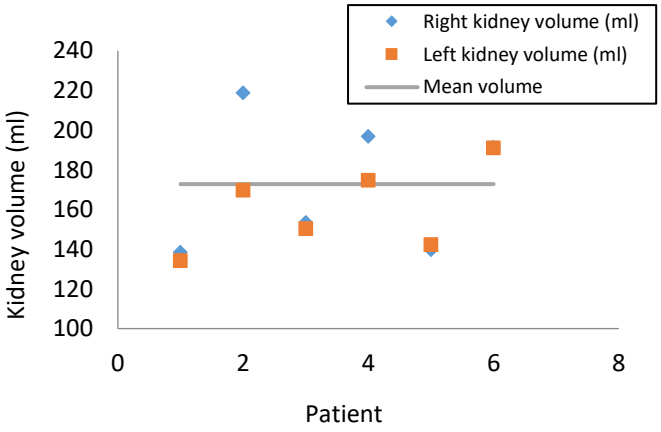

Figure 2.2: The average volume of kidney was calculated using a number of patient data sets (see also 2.7).

2.1.2 Calibration measurements

Two measurements were performed with activity concentration ratios of 1:70 and 1:68 between background and vial. During the phantom measurements, the small or medium vial was located at the bottom of the phantom. Before injecting the ^{177}Lu inside the vial, it was drawn in a syringe and diluted with pure water to reach the exact volume of each vial. Then activity of the syringe was measured using a Capintec CRC-15R Dose Calibrator (Pittsburgh, Philadelphia). As some amount of activity always adheres to the syringe wall, after injecting the activity in to the vial, the syringe was put again inside the Capintec, to obtain the exact administrated activity in phantom measurements. The calibrated activity within the small vial (25 ml) and medium vial (180 ml) was 650 and 440 MBq, correspondingly. As the time between activity injection and image scanning was about 120 minutes, the activity was measured again before initiation of the imaging.

Table 2.3: Configuration of the phantom measurements and ^{177}Lu activities inside the vials used for the calibration factor calculation.

Phantom measurement	NEMA IEC Phantom medium	Vial volume (ml)	Calibrated activity inside the vial at the time of measurement (MBq)	Activity concentration (MBq ml^{-1})	Calibrated activity in phantom (background) (MBq)
A	Without water	25	641.26	25.7	*NA
B	Water	25	641.26	25.7	0
C	Water	25	72.5	2.9	0
D	Water	25	32.4	1.3	0
E	Water	180	437.16	2.4	0
F	Water	180	437.16	2.4	1:70
G	Water (see F, after 7 days)	180	234.5	1.3	1:68

*NA: Not Applicable

2.1.3 Estimating the calibration factor by defining volume of interest (VOI)

The scatter correction method (TEW) was performed on two photopeak energies of ^{177}Lu: 113 keV with 20% width and 208 keV with 12% width. For the lower photopeak energy, the upper scatter window (USW) and the lower scatter window (LSW) width was 13% and 20%, respectively. The scatter energy window for the higher photopeak energy was set to 9% and 12.4% for USW and LSW, respectively. In Table 2.4, the energy window settings used in this work are compared to those reported in literature [14, 21, 24, 25, 27, 28, 78].

2.1.3 Estimating the calibration factor by defining volume of interest (VOI)

The total counts are normally obtained from a VOI defined in the images. Then the CF expressed in units of counts per second (cps) per MBq can be calculated as

$$CF\ (cps\ MBq^{-1}) = \frac{C}{A}, \qquad (2.1)$$

where C is the total count rate in the images (cps); A is the calibrated activity (MBq) at the measurement time within the individual VOI (large, small).

In our measurement, the VOIs were delineated in two ways: (1) A large volume which covered the known geometrical size of each vial (Figure 2.3); and (2) A small spherical volume at the center of each vial (i.e. 15% volume of each vial: 3.75 ml for small vial and 27 ml for medium one) for reducing the influence of the partial volume effect at the edge of the vial [79]. The value of count rates for the large and small volume is denoted as C_L and C_S.

The VOI was defined by using PMOD software (PMOD Technologies LLC, Zurich). For each of the photopeak energy windows (113 keV and 208 keV) and for medium and small vials, the CF was calculated, independently, resulting in 14 values of CF for small and large VOIs, separately.

2.1.3 Estimating the calibration factor by defining volume of interest (VOI)

Table 2.4: Energy window settings used in current and previous works

Publication	113 keV photopeak	208 keV photopeak
This work (clinical setting)	MW: 100.8-123.2 keV (20%) LSW: 84-101 keV (20%) USW: 123-140 keV (13%)	MW: 195-220.48 keV (12%) LSW: 172.2-195 keV (12.4%) USW: 220.48-241.28 keV (9%)
Sandström et al. [25]	MW: 100.8–123.2 keV (20%)	MW: 187.2–228.8 keV (20%)
Sanders et al. [21]	MW: 100.8–123.2 keV (20%) LSW: 84.0–100.2 keV (15%) USW: 123.2–140.0 keV (15%)	MW: 187.2–228.8 keV (20%) LSW: 145.6-187.2 keV (20%) USW: 228.8–270.4 keV (20%)
Delker et al. [14]	NA	MW: 192.4-223 keV (15%) LSW: 157.25- 182.75 keV (10%) USW: 228-252 keV (10%)
Robinson et al. [78]	MW: 100.8–123.2 keV (20%) LSW: 95.0–100.8 keV (3%) USW: 125.1–132.9 keV (3%)	MW: 187.2–228.8 keV (20%) LSW: 175.6-186.4 keV (3%) USW: 229- 243.1 keV (3%)
D'Arienzo et al. [27]	MW: 104.5–121.5 keV (15%) LSW: 93.2–104.5 keV (10%) USW: 121.5–132.8 keV (10%)	MW: 187.2-228.8 keV (20%) LSW: 164.4- 187.2 keV (10%) USW: 228.8-249.6 keV (10%)
Uribe et al. [28]	NA	MW: 187.2-228.8 keV (20%) LSW: 153- 187 keV (22%) USW: 229.5-280.2 keV (22%)
De Nijs et al. [24]	MW: 1001.7–124.3keV (20%) LSW_{wide}: 91.7–101.7 keV (10%) USW_{wide}: 124.3–134.3 keV (8%) LSW_{narrow}: 97.7–101.7 keV (4%) USW_{narrow}: 124.3–128.3 keV (3%)	MW: 187.6-229.2 keV (20%) LSW_{wide}: 177.6- 187.6keV (5%) USW_{wide}: 229.2-239.2 keV (4%) LSW_{narrow}: 183.6- 187.6keV (2%) USW_{narrow}: 229.2-233.2 keV (2%)

MW: main window; LSW: lower scatter window; USW: upper scatter window; NA: not applied

2.2 Simulation using a Monte Carlo method- SIMIND

Afterward, by using the results of phantom measurements in water as listed in Table 2.3 (B-G), a mean calibration factor (mCF) for large and small VOIs was calculated independently, and the relative uncertainty (D%) of mCF was calculated as a ratio of the difference between calibrated activity and measured activity using:

$$D\ \% = \frac{Calibrated\ activity\ (MBq) - Measured\ activity\ using\ mCF(MBq)}{Calibrated\ activity\ (MBq)} \times 100, \quad (2.2)$$

The activity is the activity in the used volume of interest.

In the case of background activity, a hot spot near the lid of the phantom was observed in the SPECT image (Figure 2.1: b) as the activity did not distribute homogenously inside the phantom. Therefore, the activity of the background had to be calculated considering the counts in the hot spot and the rest of the phantom body excluding the vial.

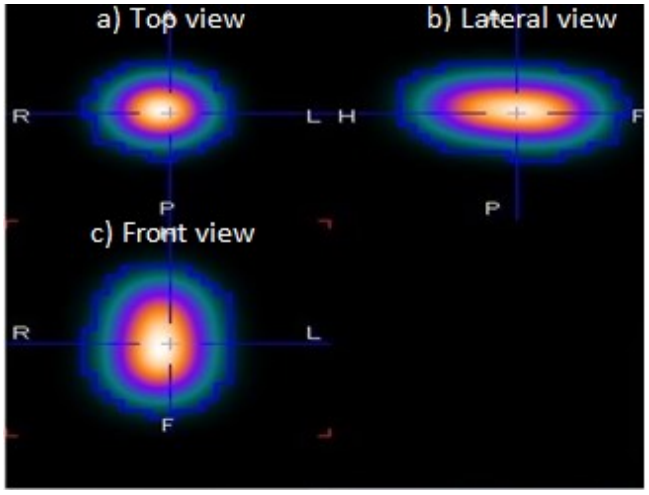

Figure 2.3: Large volume covered the geometrical size of the vial.: a) Top view, b) Lateral view , and c) Front view.

2.2 Simulation using a Monte Carlo method- SIMIND

SIMIND is a Monte Carlo based code that has been developed by Ljungberg and Strand [32]. It has been established to describe and simulate a standard clinical SPECT

camera. In addition, this program can be easily modified for other type of calculation or measurement happened in SPECT imaging. The entire code is written in FORTRAN-90 and is operated on various systems like Linux systems (x86), Mac systems running OSX, and on Windows (x86).

As explained in backgound section, the advantage of using Monte Carlo code is the capability to flag and study the parameters which degrade the SPECT images quantification. The first step in simulation is identifying the source properties and imaging system. This process is performed using "CHANGE" program, a part of SIMIND, to transfer input parameters to an external data file, named "simind.smc". This program allows user to specify different parameters to describe the desired system and conditions [72, 80].

For simulating a voxel-based phantom, the phantom by default is aligned in the *x* axis. A source which includes the administrated activity can be as same as phantom or can be defined separately. Then for simulating the SPECT, the camera rotation will be around the y and z axis either in clock-wise or counter clock wise direction (Figure 2.4).

In the CHANGE's main window there are various options that can be defined by user manually such as the phantom wall material. The phantom tissue, bone or soft tissue is expressed by a series of energy table which are used considering the cross-sectional values for the photoelectric, Compton, coherent, and pair production interactions by the individual phantom. As an example, the typical phantom cross section is water, given by the file named h2o.cr3 [34].

To describe a single or multi gamma photopeaks emitter, SIMIND has specific commands which should be used in source description. Moreover, to obtain the true values of the camera sensitivity and correct the pixel values in the projection data, the activity of the source distribution also should be defined.

2.2 Simulation using a Monte Carlo method- SIMIND

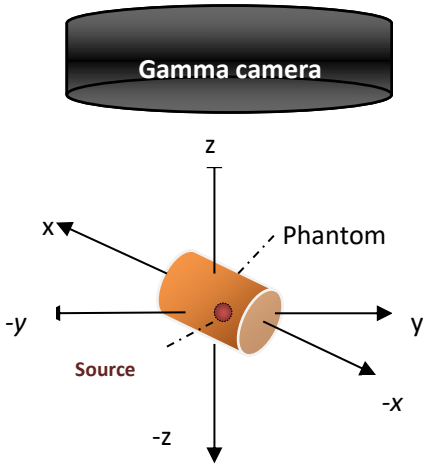

Figure 2. 4: A schematic of the phantom, source and camera directions in CHANGE program [72].

To create the projection image, the area of the collimator crystal is outlined by inserting the pixel size. However, zooming in/out the simulated image is possible by changing the value of the pixel size (smaller or larger). The matrix size of the projected image is always centered on the cylindrical axis of the crystal and no translation can be made. In the next chapter, the parameters which have been used in this project will be explained in detail.

In this work, the Monte Carlo simulation code SIMIND [72] was utilized to generate source distributions which are similar to our phantom measurements and to analyze the factors affecting reproducibility of the CF. In the simulation, a 9.7-liter cylinder phantom containing a 25 ml vial with 650 MBq of ^{177}Lu was used. To cover the principal energies needed for imaging, the full energy spectrum of ^{177}Lu from 54 keV to 250 keV was used in the simulation (Figure 2.5). In addition, a NaI(Tl) crystal with 1.54 cm thickness and a medium energy collimator were used in the simulation to mimic the detector. The energy resolution of the gamma camera was set to 9% FWHM at 140 keV, and the number of simulated projections was set to 128 in a 360° full rotation mode. All image reconstructions were made using an iterative OSEM

algorithm including the CDR function, AC and SC as in the experimental study developed by Frey et al. [34]. The reconstruction was done using 15 iterations to exclude the noise by increasing the number of iterations. However, to simulate the SPECT imaging condition, after the reconstruction, the poise noise was added to the final images. The number of subsets was eight, similar to the phantom measurement reconstruction setting.

For estimating SC, either the TEW correction for the relevant main energy windows or the effective scatter source estimation (ESSE) based on a material dependent scatter kernel [34], was applied. The collimator detector response (CDR) and AC were implemented in both correction methods.

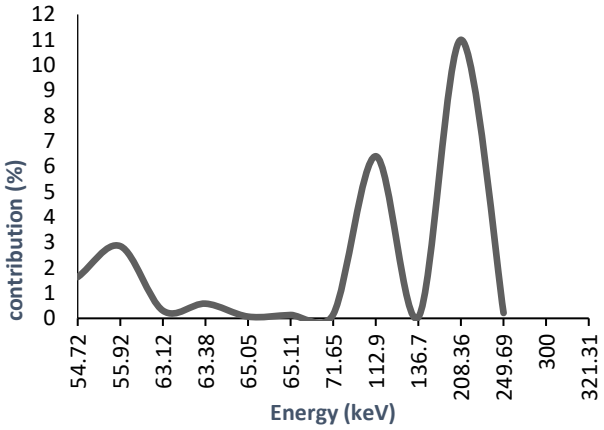

Figure 2.5: Full decay spectra of ^{177}Lu were used for simulation to include the principal energy used for imaging and those energies which are important for the component of septal penetration in the projection images.

Because the AC for ^{177}Lu depends on the scaling between transmission and emission energies, different attenuation maps were generated at 190 keV (which was used in the clinical setting as default energy), 113 keV, 208 keV, and at the weighted energy, i.e. 175 keV, of ^{177}Lu [81].

The weighted energy of ^{177}Lu ($\bar{E}_{weighted}$) was calculated as

$$\bar{E}_{weighted} = \frac{\delta_{low\ photopeak} \times E_{low\ photopeak} + \delta_{high\ photopeak} \times E_{high\ photopeak}}{\delta_{low\ photopeak} + \delta_{high\ photopeak}}, \quad (2.3)$$

where, δ with the subscript low/high photopeak represents the abundance of low/high photopeak energy of ^{177}Lu.

As shown in Figure 2.6, the attenuation map (AM) was created using CT images of SPECT/CT based on a standard model proposed in [82].

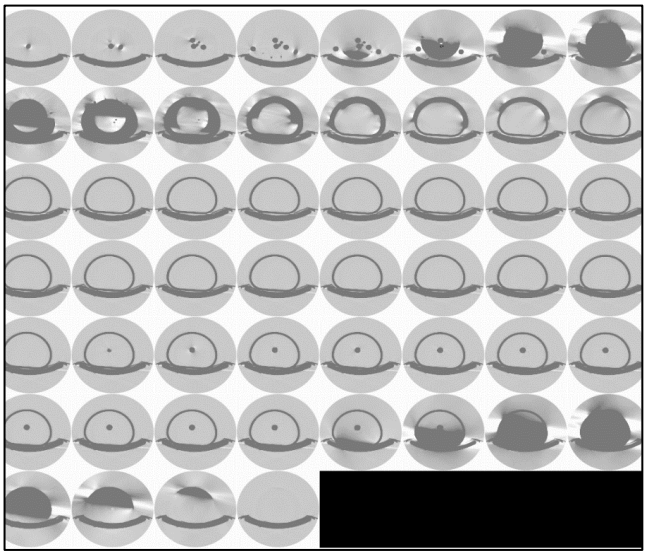

Figure 2.6: Created attenuation map (AM) for attenuation correction.

Calibration from Hounsfield units to attenuation coefficient was made by scaling the units related to the main photopeak energy and the phantom medium. For this purpose, a bilinear model that describes the linear attenuation coefficient conversion ratio for air-and-water and water-and-plexiglass was used [82]:

$$\mu_{air+water,E} = \frac{CT_{H.U} \times \{\mu_{water,E} - \mu_{air,E}\}}{1000}, \quad (2.4)$$

$$\mu_{water+plexiglass,E} = \mu_{water,E} + \frac{CT_{H.U} \times \mu_{water,E_{eff}} \times \{\mu_{plexiglass,E} - \mu_{water,E}\}}{1000 \times \{\mu_{plexiglass,E_{eff}} - \mu_{water,E_{eff}}\}}, \quad (2.5)$$

where, $CT_{H.U}$ is the value of CT number in the Hounsfield unit, μ is the target translated emission energy and E_{eff} is the effective X-ray photon energy.

The linear attenuation coefficients μ (cm^{-1}) in water and plexiglass (the NEMA IEC body phantom housing) were estimated as a function of photon energy. In addition, the relative uncertainty of calculated CFs between applying the AC at above mentioned energies was determined.

The influence of scatter window width on the TEW method was studied by varying the lower and upper scatter windows. To apply the TEW correction, the following equation for the relevant main energy window was used:

$$C_{Primary} = C_{total} - 0.5 \times \left(\frac{C_{LSW}}{W_{LSW}} + \frac{C_{USW}}{W_{USW}}\right), \quad (2.6)$$

where, $C_{Primary}$ is the total counts of the primary photons in the main energy window, C_{LSW} and C_{USW} are referred to the counts in the lower and upper scatter energy windows, respectively. The W_{LSW} and W_{USW} are the respective widths of the corresponding scatter energy windows.

As illustrated in Table 2.4, Robinson et al. [83] used the SC windows width of ±3% for both gamma photopeaks of ^{177}Lu, which was smaller compared to other literature data. De Nijs et al. [24] tried two different SC windows for each of photopeaks. Following their idea, various scatter windows were applied to 208 keV and 113 keV ^{177}Lu photopeaks which are listed in table 2.5.

To model the ESSE correction, as a scatter correction model, two scatter kernels (k.n and k.μ_s) as the pre-calculated point-spread functions were required. The kernel k.n (the normalized scatter kernel) is an image whose values are the probability that a photon emitted at the center of the kernel will have its last scatter event inside the voxel of interest and be detected, excluding the probability of attenuation along the path from

the voxel of interest to the detector. The kernel $k.\mu_s$ represents the weighted average attenuation coefficient in water after the last scatter event for all photons whose last scatter event occurs in the corresponding voxel. These two scatter kernels were computed using the SIMIND Monte Carlo code and then combined together to be used in image reconstruction. Since these kernels have cylindrical symmetry about the line through the source that is perpendicular to the detector, only one quadrant of the kernel was stored in the direction parallel to the detector. The kernel was stored so that slices were parallel to the face of the collimator with slice 0 being furthest away and the last slice being closest. The source location was in pixel (0,0) in slice *N/2*-1, where *N* was the number of slices in the kernel. Besides, the photons were tracked through a slab phantom. A modified score routine takes over when the photon is terminated. During tracking, the track of the last scatter point and the attenuation coefficient after scattering was kept at this point. For each photon, the weight, w_i (which is the total probability that a photon travels the given path and reaches the detector) was summed into a 3D image at the position corresponding to the last scatter point. In addition, the attenuation factor from the last scatter point was calculated as [57]

$$Attenuation\ factor = e^{-\mu_i x_i}\ , \tag{2.7}$$

where, μ_i is the attenuation coefficient and x_i is the distance from the last scattering point to the surface of the slab for the *i*th photon.

After tracking all the photons, a new image was computed by SIMIND referred as the average attenuation factor image. This image represented the average attenuation factor for all photons having their last scattering event in a given voxel, weighted by the kernel contribution. Then the kernel image (*k.sim*) and average attenuation factor image (*af.sim*) were saved. In order to use these images, in the ESSE scatter model, it was necessary to (1) normalize the kernel image (per emitted photon) and (2) convert the average attenuation factor image to an average attenuation coefficient image. To

accomplish the normalization, the *k.sim* image divided by the number of detected photons in air. The computation of the attenuation factor for each last scattering voxel from the *af.sim* image was done by

$$\mu_{si} = -\ln(af_i)/xi\ , \tag{2.8}$$

where μ_{si} is the kernel of μ image needed for ESSE modeling, af_i is the average attenuation factor (from the *af.sim* image) value for the same pixel, and *xi* is the distance for that pixel to the surface of the phantom (Figure 2.7).

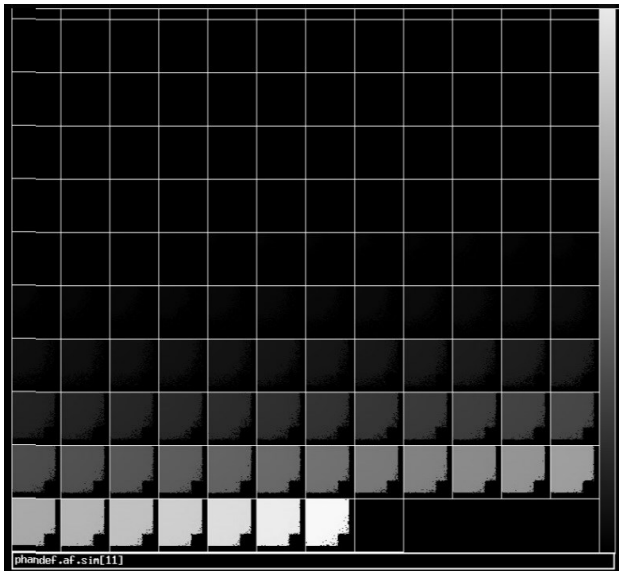

Figure 2.7: The kernel images were created to use for ESSE modeling.

Because ^{177}Lu has two main gamma photopeak energies, to normalize the scatter kernel, the number of detected photons in air was estimated. Then the scatter and attenuation kernels from the multiple windows into a single file were combined which was used for image reconstruction. As a reference, a CF was calculated for simulations in which only non-scattered events were taken into account, and the AC was applied

using an attenuation map at the energy of 190 keV. The total counts inside the large VOIs were used to calculate this factor.

The SCF was calculated for each of the scatter energy windows (Table 3.3) following MIRD No. 26 [4]

$$SCF = \frac{Total\ scattered\ photons\ estimated\ by\ the\ TEW}{Total\ photons\ in\ main\ energy\ window\ before\ any\ correction}. \quad (2.9)$$

An ideal scatter correction should exclude the detected scatter photons in the main energy window. After an appropriate scatter correction, the voxel values should be equal to the number of geometrically collimated detected photons which are emitted from the activity source (vial) with negligible scattering and attenuation. For this reason, an actual scatter fraction was determined as

$$ASCF = \frac{Total\ scattered\ photons\ in\ the\ main\ energy\ window\ before\ any\ correction}{Total\ photons\ in\ main\ energy\ window\ before\ any\ correction}. \quad (2.10)$$

To investigate the accuracy of the SC, for all combinations of scatter energy windows, the SCF was determined and compared to ASCF. The deviation of the SCF from the ASCF was estimated to evaluate the SWs effect on the scatter correction.

The collimator detector behavior related to the source distance and energy was also simulated. As explained in section 1.5.3, for SPECT imaging system, a CDR contains 4 main concepts named as: intrinsic geometric, septal penetration and septal scatter responses. Hence due to the full width at half maximum (FWHM) of each photopeak energy a full CDRF was generated (Figure 2.8 and Figure 2.9) for a point source in various distances from the surface of the collimator: 2, 5, 10, 15, 20, 30, 40 and 60 cm using the clinical setting for the main photopeak energy windows of ^{177}Lu (113 keV with 20% width and 208 keV with 12% width).

Table 2. 5: Different combination of scatter windows which used during TEW modeling.

scatter energy windows for the 113 keV photopeak energy		
1(clinical setting)	84-100.8	123.2-140
2	84-100.8	123.2-175
3	74-100.8	123.2-140
4	74-100.8	123.2-150
5	74-100.8	123.2-170
6	54-100.8	123.2-133.2
7	54-100.8	123.2-170
8	54-100.8	123.2-140
9	90.8-100.8	123.2-133.2
scatter energy windows for the 208 keV photopeak energy		
1(clinical setting)	172.2-195	220.48-241.28
2	142-195	220.4-271.2
3	162-195	220.4-251.4
4	190-195	220.48-225.48
The width of the main photopeak energy window in all combinations was 100.8 keV-123.2 keV and 195 keV-220.4 keV for 113 and 208 keV, respectively.		

In SIMIND, by increasing frequency of repetition, probable errors can be decreased. Thus, we generated a CDRF table by simulating 20 seeds for each photopeak energy and photon category (primary or scattered photons). A point response (PR) and geometric point response functions (GPR) were simulated at various source-to-camera distances: 2, 5, 10, 15, 20, 30, 40 and 60 cm in air. The GPR function is a distribution of photons on the surface of the detector. It is determined by geometrical space of the collimator holes. In the simulation directory, two directories were created named as: infile and script. The infile directory had the input files required for the simulation, which were included two mandatory files (*cdrf.smc, dist.csv*) and 4 optional files (*p_spectrum.isd, ergrange.csv, switch.txt and cdrf.win).*

2.2 Simulation using a Monte Carlo method- SIMIND

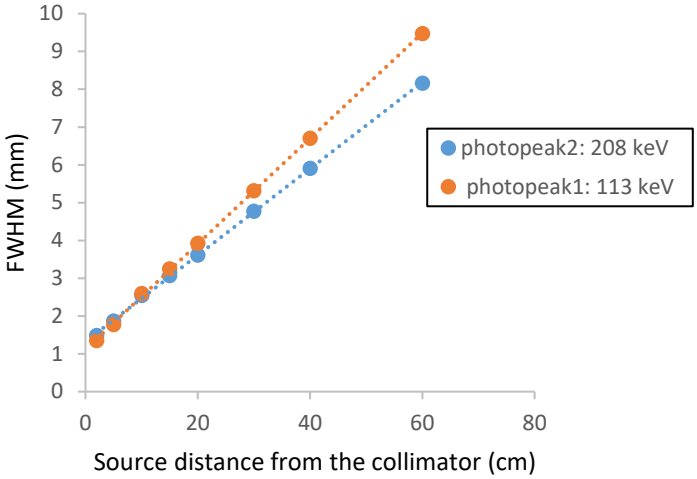

Figure 2.8: Magnitude of the Full width at half maximum (FWHM) is depended to the photopeak energy and the source distances from the surface of the collimator.

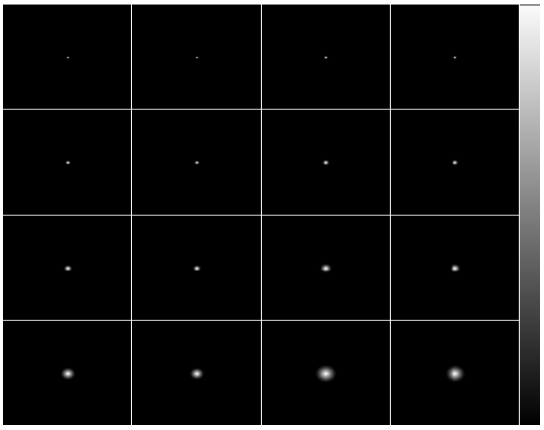

Figure 2.9: Image (point source) became blurred when the distance of the source to the collimator increased**.**

The dist.csv file (mandatory file) contained a list of the distances between the point source and the collimator face. As mentioned above the collimator detector response was simulated in different distances equal to 2, 5, 10, 15, 20, 30, 40, 60 cm. The *spectrum.isd* had to be used for simulating multiple emission energy peaks. To read

the relevant file to each photon category, the ergrange.csv file was created. Each line in this file indicates the name of a photon category (primary or scatter), and the low and high energy in keV of the corresponding energy sub-range. In this work, to cover all the emitted photons the energy range was 0-320 keV, for primary and scattered photons. Also, the *cdrf.win* file was recorded to allow simulation of PR function for multiple energy windows simultaneously. Each line in the file corresponds to each energy window. A number of important parameters used in this work, are listed in Table 2.6.

Table 2.6: Frequently used parameters by SIMIND for generating CDRF table.

Parameter	Value
Photon energy	For ^{177}Lu as a polyenergetic radionuclide, we used a negative value and input the spectrum using a spectrum file that will be described later.
Source dimensions	The simulated source had 25 ml volume.
Phantom dimensions	We simulated a 9.7-liter cylinder.
Crystal half length	40 cm
Crystal thickness	We used 1.59 cm as thickness.
Height to detector surface	We simulated a point source at multiple distances from the collimator face. A specific script file was used for this parameter.
Phantom type	Horizontal cylindrical phantom
Source type	Cylindrical bottle
Window settings	Energy window in keV (upper and lower threshold)
Energy resolution (140 keV)	9%
Number of photons x10^6	Simulation for 50000000 photons.
Pixel size	4.79 mm
Camera Offset	The half of the pixel size was used.
Collimator parameters	The MELP parameters were applied.
Move the collimator	We simulated a moving collimator.
Matrix Size	128×128

2.3 Patient study

In order to calculate the radiation absorbed doses to organ at risk like kidney and liver, the calculated mean calibration factor using large VOI from experimental measurement was used. Before radio-ligand therapy, all patients were informed about the procedure and written consent was given. ^{177}Lu-PSMA I&T administration was

approved by the local ethic committee (Ethikkommission der Fakultät für Medizin der Technischen Universität München), and in compliance with the 1964 Helsinki Declaration. The study was in accordance with German regulation (Federal Agency for Radiation Protection).

As the purpose of patient study was estimating the individual absorbed dose, the calibration factors using the large VOIs (CF_L) obtained by phantom measurements were used. Then, the average value of the calibration factor was applied to the SPECT data to estimate the activity uptake in the liver and kidneys and consequently to create the related time activity curves (TAC). Then, the absorbed doses to the target organs were calculated using OLINDA/EMX software. Indeed, the planar images were performed to compare its results with the results of the SPECT images. For planar activity quantification, a correction factor had to be calculated. Finally, the results from planar and SPECT imaging were compared and the differences were evaluated.

2.3.1 Patient data

Data sets of six patients, at their first cycles of the therapy, were analyzed comprising whole body planar and abdominal SPECT/CT imaging (one bed position) as is shown in table 2.7. All patients had histopathological diagnosis of prostate stages. The ages ranged from 66 to 78 years (mean 71±3.5 years). Patients were imaged at 5 time points (2, 24, 48, 72, and 168 hours) after start of therapy. ^{177}Lu-PSMA I&T with an activity between 6500 MBq-7200 MBq was administered per patient. Five patients had high uptake in spleen and one of them had also metastases in liver. One patient had no metastases and spleen uptake. For individual dosimetry, the volumes of the desired organs were derived from pre-therapeutic ^{68}Ga-PSMA-HBED-CC PET/CT.

2.3.2 Estimation of the activity uptake using planar images

As explained in section 1.4.1, the planar images give 2D distribution images of an administrated activity inside the patient's body. Since the images cover whole body, it makes it possible to study the activity uptake in various organs. In this work, whole-

2.3.2 Estimation of the activity uptake using planar images

body scintigraphy (planar imaging) was performed in two various views means anterior and posterior and the images were recorded between 30-120 minutes, 24, 48,72, and 168 hours after ^{177}Lu-PSMA I&T administration. Region of interest (ROI) covering the whole body, kidneys and liver were drawn at two different views (interior and posterior) using a DICOM image viewer program, OSIRIX (Pixmeo, Switzerland), and the total counts inside each organ of interest was obtained (Figure 2.10).

Table 2.7: Data set of six patients.

Patient's number	1	2	3	4	5	6
*Metastases (S,L, No)	S & L	S	S	S	S	No
Therapy cycles	First	First	First	First	First	First
Injected activity (MBq)	7019	6470	6471	7155	7170	7172
Liver volume (ml)	1581	1904	1880	1353	1321	2373
Right kidney volume (ml)	138.4	218.7	153.4	196.8	139.7	191.4
Left kidney volume (ml)	134.2	169.7	150.4	174.7	142.3	191

*S: High uptake in spleen, L: Liver metastases; No: No metastases

To convert the quantitative data to activity uptake, a correction factor had to be calculated. For this purpose, probe measurements were performed after the activity administration for each patient. Hence, before the first planar imaging, each patient was guided to a gamma probe room, where a gamma probe (detector) was positioned at a distance about of 2 meters from the patient. The patients were asked to stay in front of the detector. Then the total counts of the whole body were recorded by the detector. The second probe measurement was conducted after the first urinating, in order to analyze the variation of the calculated factor.

These measurements were repeated for each patient in one week and at least in 4 time points. To estimate the activity uptake in each individual organ, the total count inside the drawn ROIs were converted to the activity in MBq using the calculated factor.

2.3.3 Estimation of the activity uptake using SPECT images

As the administrated activity was known for each patient, the correction factor was calculated using the recorded counts in the first step as

$$correction\ factor = \frac{total\ count\ (\ anterior\ position) + total\ count\ (posterior\ position)}{administrated\ activity\ at\ the\ time\ of\ probe\ measurements\ (MBq)} / 2\ . \qquad (2.12)$$

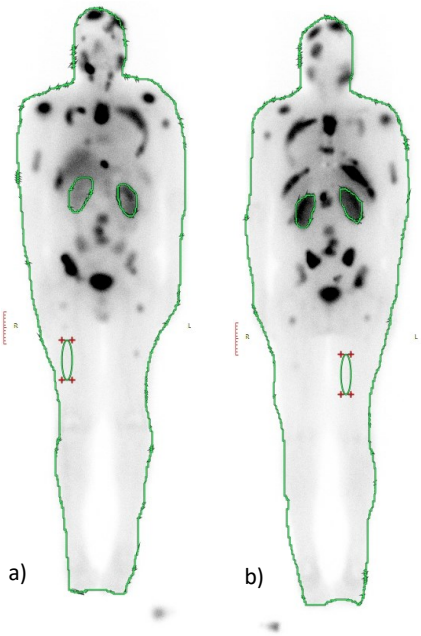

Figure 2.10: ROI for liver and kidney were drawn using planar image: a) anterior and b) posterior view.

As explained in section 2.3, the absorbed doses to the liver and kidney were calculated using OLINDA/EMX software. For personalized dose calculation, the time activity curves (TAC) of organs, the administrated activity, and the organs' volumes of each patient were used as the input data.

2.3.3 Estimation of the activity uptake using SPECT images

For each patient, VOIs were drawn for kidneys and liver in SPECT images. Similar to the planar imaging, the SPECT/CT scanning was recorded at five time points. At each time point, 81 slices were explored. Because of the half-life and the biological

2.3.4 Patient specific organ dose calculation using OLINDA/EXM software

excretion of the ^{177}Lu, at the last day of imaging (7 days after the activity administration), the uptake of the radionuclide was not clear to observe from the SPECT images and therefore an accurate contouring of target organs was not possible. Hence, by fusing SPECT images with CT images the region of target organs was drawn more accurately. (Figure 2.11).

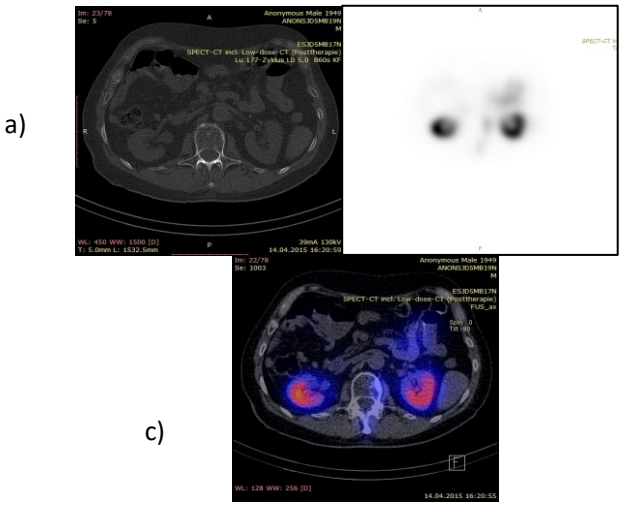

Figure 2.11: a) An abdominal CT image used to define organ, b) An abdominal SPECT image used to obtain total counts within organ, and c) SPECT/CT image fusion.

Then the total counts of VOIs were converted to the activity by using the calculated conversion factor, which is described in section 2.3.1. Indeed, for individual dosimetry, the volume of kidneys and liver were derived from the diagnostic CT to use in activity calculation (Table 2.7).

2.3.4 Patient specific organ dose calculation using OLINDA/EXM software

OLINDA/EXM is one of the most common software used for organ dose estimation [4, 20, 84]. The input data is the time activity curve (TAC). Assuming a uniform distribution in each target organ, the result will be the mean personalized absorbed

2.3.4 Patient specific organ dose calculation using OLINDA/EXM software

dose for each individual organ. This software includes different phantom models. Two parameters which need to be individually defined are 1) the organ's volume, and 2) the injected activity. These two parameters have effects on the organ dose level.

In this work, the individual dose was calculated for each patient using planar and SPECT data, separately. For this purpose, a whole-body phantom representing an adult was chosen [84] and the values of the calculated activities at different time points were uploaded to the OLINDA software, Figure 2.12.

To fit the activity time curve, an exponential model was used as

$$Activity\ (MBq) = Ae^{-at} + Be^{-bt}\ , \tag{2.13}$$

where A and B correspond to the two first measured activities for each organ, and a and b are related to the half-life of the ^{177}Lu. When the activity time curve was obtained for each patient, the individual organ volumes which had already defined from CT of PET/CT were given before dose calculation. Then, the calculated absorbed doses using SPECT images were compared with planar image results.

2.3.4 Patient specific organ dose calculation using OLINDA/EXM software

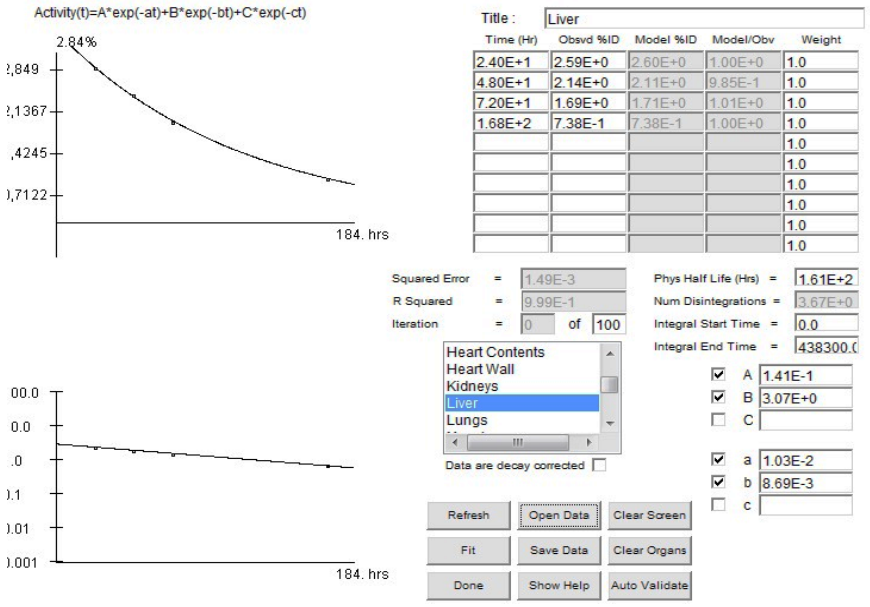

Figure 2.12: Left graphs show time-activity curves (TAC); right screen shows the activity of each organ at 4 different measured time. The imported data into the table was created using the function described in eq. 2.13.

3 Results

Part of this chapter has been published in following publications:

- Karimi Ghodoosi, E., D' Alessandria, C., Li, Y., Bartel, A., Köhner, M., Höllriegl,V., Navab, N., Eiber, M., Li, W.B., Frey, E., Ziegler, S. (2018): The effect of attenuation map, scatter energy window width, and volume of interest on the calibration factor calculation in quantitative ^{177}Lu SPECT imaging: Simulation and phantom study. Physica Medica 56, 74-80
- Karimi Ghodoosi, E., D'Alessandria, C., Eiber, M., Li, W.B., Navab, N., Ziegler, S.: Comparison of absorbed dose to kidneys using quantitative SPECT/CT and whole body planar images for Lu-177-PSMA I&T in prostate cancer therapy. Eur. J. Nucl. Med. Mol. Imaging 45, S112-S113 (2018)

3.1 Phantom measurements

The aim of the phantom measurements was to calculate a calibration factor for estimating the amount of organ activity from quantitative SPECT/CT images which were used for individual dosimetry in clinical measurements. Consequently, in this work, the mean CF by different phantom measurements was used to contribute the results of two different vials (25 and 180 ml) and to investigate the difference between the measured activity and administrated activity, in case a unique calibration factor for different objects is used. Moreover, by each measurement, the calibration factor was calculated for each of the gamma photopeak energy of ^{177}Lu. The calculation of the mean calibration factor was carried out using the results of both photopeak energies to investigate the influence of contribution of both photopeaks on the activity estimation. To study the effect of the activity background on the CF calculation, a specific amount of background was injected to water-filled phantom including the 180 ml vial. As the

background was not distributed uniformly inside the NEMA IEC phantom, the impact of the ununiformed distribution on the activity estimation was also explored.

In order to investigate the influence of VOI on calibration factor calculation, partial volume effect, and consequently on activity estimation, the VOIs were drawn in two ways: 1) large and 2) small VOIs. As explained in section 2.1.3, the large VOI covered the vial geometric completely; in contrast, by drawing the small VOI, 15% of the object volume was enclosed including the voxel with maximum intensity. The results of CF_L numbers calculated by the phantom measurements using large VOIs in water by applying different activity concentrations and volumes are shown in Figure 3.1. For the 25 ml vial with varying activity concentrations: 1.3, 2.9 and 26 MBq ml^{-1} the calculated calibration factor using large VOIs was about 1.5±0.2 cps MBq^{-1} and 2.2±0.1 cps MBq^{-1} for the 113 keV and the 208 keV, correspondingly. Likewise, for the 180 ml vial, the CF_L using different activity concentrations, with/out background, was calculated. By using 1.3 and 2.4 MBq ml^{-1} activity concentrations, similar to the results for 25 ml vial, the variations of the CF_L for both gamma photopeak energies, were negligible. For the low and high photopeak energies, the CF_L was calculated as 2.3±0.06 and 2.97±0.1 cps MBq^{-1}, respectively.

The CF_L for the 25 ml and 180 ml vials, using the same activity concentration (in this work 1.3 MBq ml^{-1}) reveals the object volume effect on the ^{177}Lu activity quantification. Using the 180 ml vial, representing a kidney, the CF_L was increased to 55 and 38 %, for the 113 and 208 keV photopeak energies correspondingly. Also, the calculated CF_L considering both photopeak energies was 37% higher for the 180 ml vial than for the 25 ml vial. Since, the phantom measurement in air was performed only for 25 ml, its result was not contributed to the mean CF_L calculation. From the 6 measurements in water, the calculated mean CF_L for the water-filled phantom was 1.9 cps MBq^{-1} and 2.6 cps $MBq^{-1}$for the 113 keV and the 208 keV photopeak energy

of ^{177}Lu, respectively. The average mCF_L across energy windows and vial size was 4.5±0.8 cps MBq^{-1}.

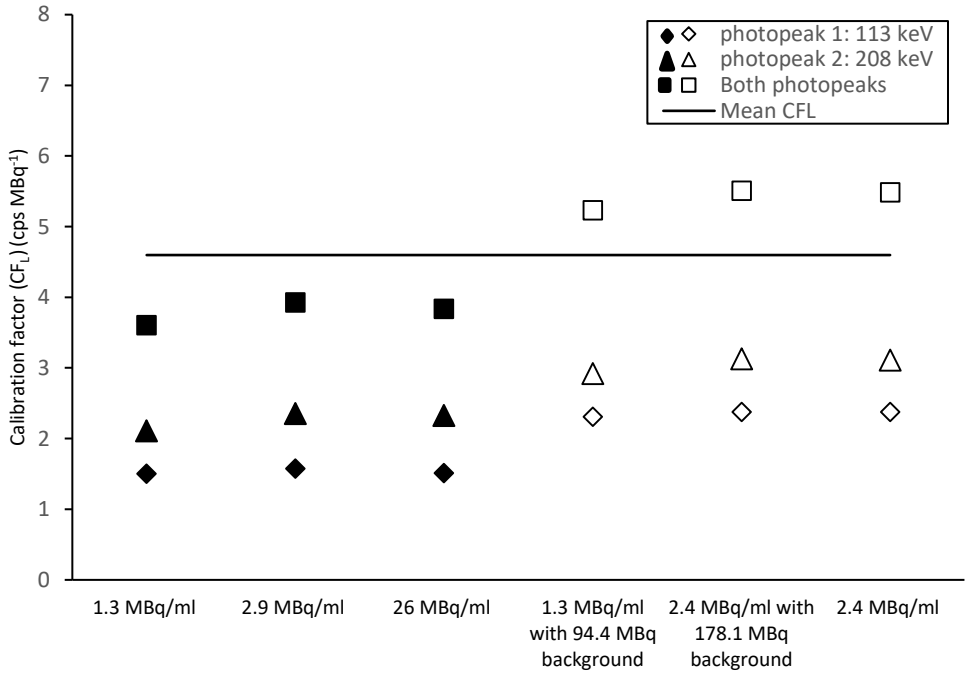

Figure 3.1: The calculated calibration factor using large VOIs for each photopeak energy window with various activity concentrations of ^{177}Lu-PSMA I&T in a 25 ml vial (filled symbols) and a 180 ml vial (open symbols) representing a lesion and a kidney, respectively.

By using the small VOIs, for the 25 ml vial the CF_S numbers was calculated as 1.64±0.04 cps MBq^{-1} for the low photopeak energy and 2.5±0.02 cps MBq^{-1} for the high photopeak energy. The value of calculated calibration factor for the vial with 180 ml was 2.32±0.078 and 3.14±0.012 cps MBq^{-1} for low and high photopeak energy, respectively. Using 6 phantom measurements in water, the mean calibration factor

(mCF_S) for both photopeak energies was calculated as 4.8±0.72 cps MBq^{-1} (Figure 3.2). It was observed that by using a same activity concentration (e.g.1.3 MBq ml^{-1}), for the 180ml vial, the calculated CF_S was 32 and 26% higher than the small vial for the 113 keV and 208 keV photopeak energies, correspondingly. Although the calibration factors for the medium vial were still larger than the small vial, the differences had a reduction of 23 and 12% compared with large VOIs for low and high photopeak energies, respectively.

To convert the count rates inside the VOIs into the true activity, the mean calibration factor was used. The activity was calculated using the mean calculated calibration factor over the large and small VOIs (mCF_L and mCF_S) separately. Then the estimated activity was compared to the calibrated activity at the time of measurement. As shown in Table 3.1 (A), the deviation of the measured activity by SPECT from the calibrated activity for the 25 ml vial in air including 641.26 MBq of ^{177}Lu was 12% and 8% by using the mCF_L and mCF_S, respectively.

In the absence of the activity background, for the 180 ml vial including 437.16 MBq of ^{177}Lu in water-filled phantom, the activity was calculated as 527.40 and 463.48 MBq by using mCF_L and mCF_S, correspondingly. Consequently, the related deviation from the calibrated activity was calculated as 21% and 6%. In contrast, in the presence of background (178.1 MBq of ^{177}Lu-PSMA I&T), the measured activity for the large VOI was 17% and for the small VOI was 13% higher than the calculated activity without background. Besides the vial activity measurement, the activity of the background was also calculated by mCF_L and mCF_s independently. Using the mCF_L, the sum of the activity of the hot spot near the lid of the phantom and the rest activity inside the phantom was 160.13 MBq which was 11% lower compared to the 178.1 MBq calibrated injected activity.

However, by using the mCFs, the total activity was calculated as 177.64 MBq with the deviation about 1% from the administrated activity. In the presence of 178.1 MBq of ^{177} Lu as background, the calculated activity was only 1% greater than the measured activity in the absence of the background either using mCF_L or mCF_S (Table 3.1*:* E and F).

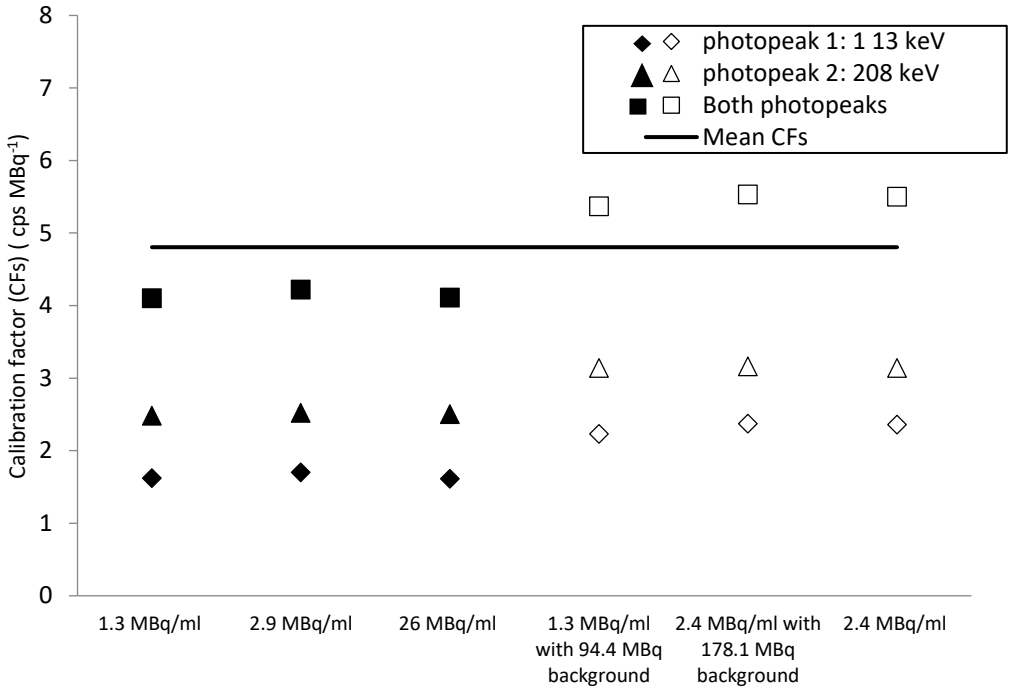

Figure 3.2: The calculated calibration factor using small VOIs for each photopeak energy window with various activity concentrations of ^{177}Lu-PSMA I&T in a 25 ml vial (filled symbol) and a 180 ml vial (open symbol) representing a lesion and a kidney respectively.

Table 3.1 SPECT phantom validation measurements using mean CF based on two different VOIs.

Phantom measurement procedure (section 1.2)	Calibrated activity at the time of measurement (MBq)	Measured activity by SPECT (MBq) using mean CF from large VOI	Measured activity (MBq) by SPECT using mean CF from small VOI
A	641.3	528.5 (D* = -17.6)	591.4 (D = -7.8)
E	437.2	527.4 (D = +21)	463.5 (D = +6)
F**	437.2	536.8 (D = +22)	469.5 (D = +7.5)
G	234.5	279.1 (D = +19)	257.5 (D = +9)

* represents the percentage variation of the measured activity from the known activity;
** water-filled phantom with 178.1 MBq activity background

Similarly, 7 days after filling the phantom with 178.1 MBq of ^{177}Lu-PSMA I&T, the activity of the 180 ml vial with 1.3 MBq ml^{-1} activity concentrations was calculated again. The variation of the measured activity from the calibrated activity was 19 and 9% using large and small VOI, respectively (Table 3.1: G).

3.2 Simulation using the SIMIND Monte Carlo code (SMIND)

In this work the simulations were applied based on the SIMIND Monte Carlo code to investigate the effect of the scatter correction (SC) method, scatter energy window (SW) width, attenuation map, and the collimator detector response (CDR) on the calibration factor calculation. In order to evaluate the clinical settings which were used in phantom measurements, the calculated calibration factor using the simulated phantom was compared to the result of the experimental measurements. Hence, under the same condition as the phantom measurement, the simulations were carried out by generating a 9.7 liter cylinder phantom containing a 25 ml cylinder source with a homogenous distribution of 650 MBq (26 MBq ml^{-1}) of ^{177}Lu (Figure 3.3).

3.2 Simulation using the SIMIND Monte Carlo code (SMIND)

Then the phantom measurements were simulated over different scatter energy windows width. Moreover, the effects of generated attenuation map at different energies and also collimator detector response compensation were studied by calculating difference in the value of CF.

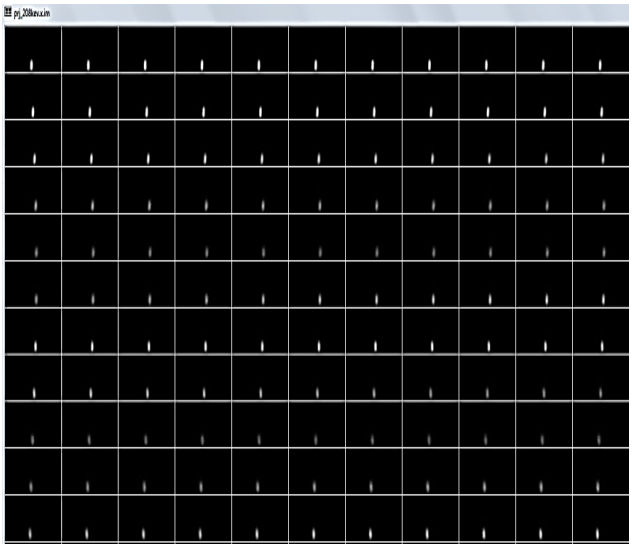

Figure 3.3: Simulated cylinder phantom including a 25 ml vial with 650 MBq of ^{177}Lu in water.

Before image reconstruction, the different photon transactions with collimator and phantom media were characterized for both gamma photopeak energies. Hence, the geometric, penetration, septa penetration, and scatter components of both photopeaks of ^{177}Lu events were investigated to determine the significance of collimator interactions (Table 3.2). As described in section 1.3.3, the geometrical collimated photons are referred to the photons which are crossed through the collimator hole without interaction. The penetration implies penetration of one or more septa, and scatter is defined as the scattering in the collimator lead. The outputs were divided in two groups: with or without backscattering from the compartment behind the crystal.

The backscatter phenomenon is due to the gamma rays of the activity source which are Compton scattered by materials in the area of the detector. When a gamma ray is scattered in the backward direction, it gives most of its energy to the electron that it

interacts with, but it still retains some of its energy. If this reduced-energy gamma ray is detected by the scintillation detector, it will interact with the scintillation crystal in the same way as a primary gamma ray emitted by the detector. This means that Compton scattered gamma rays from surrounding materials have a minimum energy when they are scattered back to the detector. As shown in table 3.2, the contribution of the scatter photons by the septa penetration is considerable only for the 208 keV gamma rays. In contrast, the number of detected photons by the crystal, after backscattering were more for the low energy photons (113 keV).

In addition, separated images for each gamma photopeak were generated to visualize the results shown in table 3.2. In figure 3.4, events from geometrical collimated primary attenuated photons from the phantom have the maximum contribution to the final image.

As explained in section 2.2, to reconstruct the simulated phantom two different scatter correction methods were applied: (1) TEW and (2) ESSE. The CDR and attenuation correction (AC) were applied for both techniques.

In order to compare two scatter correction methods (TEW and ESSE) and to assess their impact on computing the calibration factor, a reference CF for the water-filled phantom was calculated. For this purpose, all detected photons excluding scattered events were included in calculation. The value of the reference CF was obtained as 3.3 cps MBq^{-1}. Using the ESSE method applied to all detected photons, the CFs in water and air were 3.4 and 3.2 cps MBq^{-1}, respectively. However, by applying the TEW as a correction method, the CF was 4.0 cps MBq^{-1} in water and 3.0 cps MBq^{-1} in air, comparing these findings to the ESSE method results, the CF was 17% higher in the water-filled phantom and about 6% lower in air (Figure. 3.5).

3.2 Simulation using the SIMIND Monte Carlo code (SMIND)

Table 3.2: Contribution of gamma photopeak energy of ^{177} Lu in different events in the detector crystal.

With no backscatter from the compartment behind the crystal						
	Events from geometrical collimated primary attenuated photons from the phantom	Events from penetration of a septa from primary attenuated photons from the phantom	Events from scatter from the collimator from primary attenuated photons from the phantom	Events from geometrical collimated from scattered photons from the phantom	Events from penetration of a septa from scattered photons from in the phantom	Events from scatter from the collimator from scattered photons from the phantom
208 keV	85054	445.37	160.3	42835.7	227	56.2
113 keV	58985.9	0	0	97696.4	0	0
With backscatter from the compartment behind the crystal						
	Events from geometrical collimated from primary attenuated photons from the phantom	Events from penetration of a septa from primary attenuated photons from the phantom	Events from scatter from the collimator from primary attenuated photons from the phantom	Events from geometrical collimated from scattered photons from the phantom	Events from penetration of a septa from scattered photons from in the phantom	Events from scatter from the collimator from scattered photons from in the phantom
208 keV	3.8103	1.1	0	2.1	0	0
113 keV	62.8	0	0	23.2	0	0

3.2 Simulation using the SIMIND Monte Carlo code (SMIND)

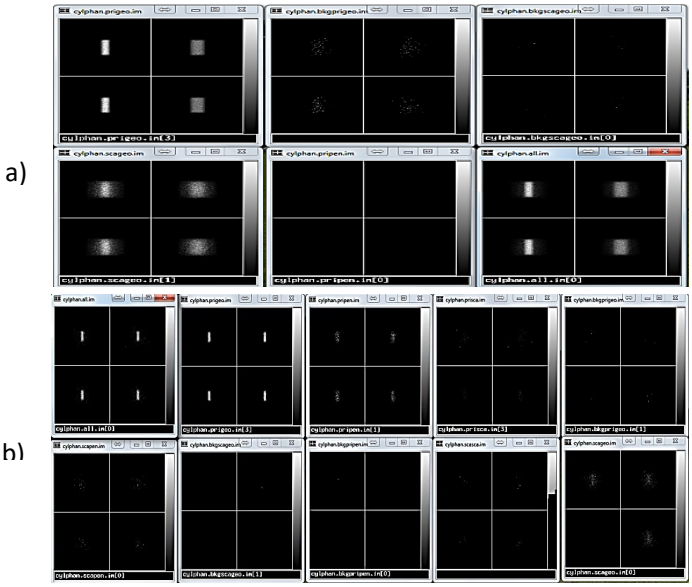

Figure 3.4: Contribution of various events with collimator and phantom medium: a) low photopeak energy (113 keV) and b) high photopeak energy (208 keV).

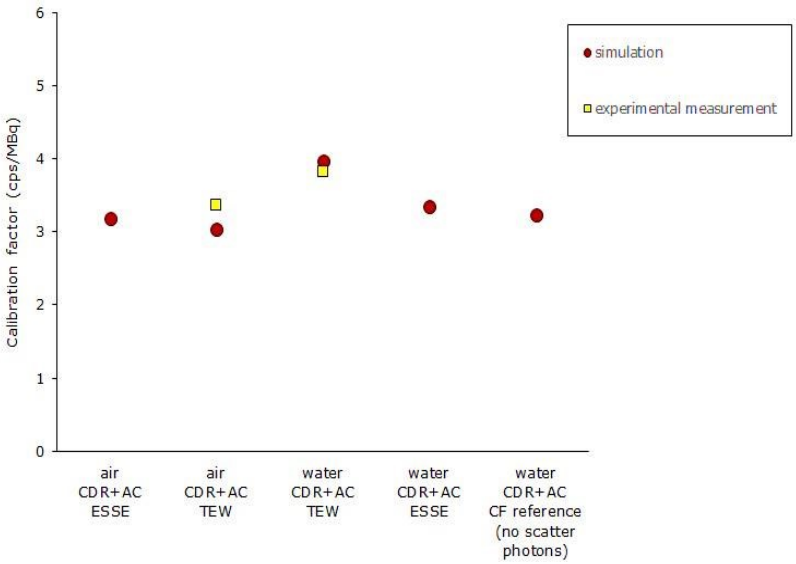

Figure 3.5: Different scatter correction (SC) methods: the triple energy window (TEW) and effective scatter source estimation (ESSE) during simulation in water and air, compared to experimental measurements. The collimator detector response (CDR) and attenuation correction (AC) were implemented in all simulations.

3.2 Simulation using the SIMIND Monte Carlo code (SMIND)

To generate the AM for AC, the linear attenuation coefficients in water and Plexiglas were calculated for each of gamma photopeak energies, the weighted energy of ^{177}Lu (175 keV) and ^{81}Kr (190 keV), separately. The results showed that the attenuation correction which was applied based on 175, 190 instead of 113 keV, for the low photopeak energy, caused -23 and -30% differences in CF calculation. Meanwhile, for the high photopeak energy, this difference was +24% and +12% for the 175 keV and 190 keV, respectively (Figure 3.6).

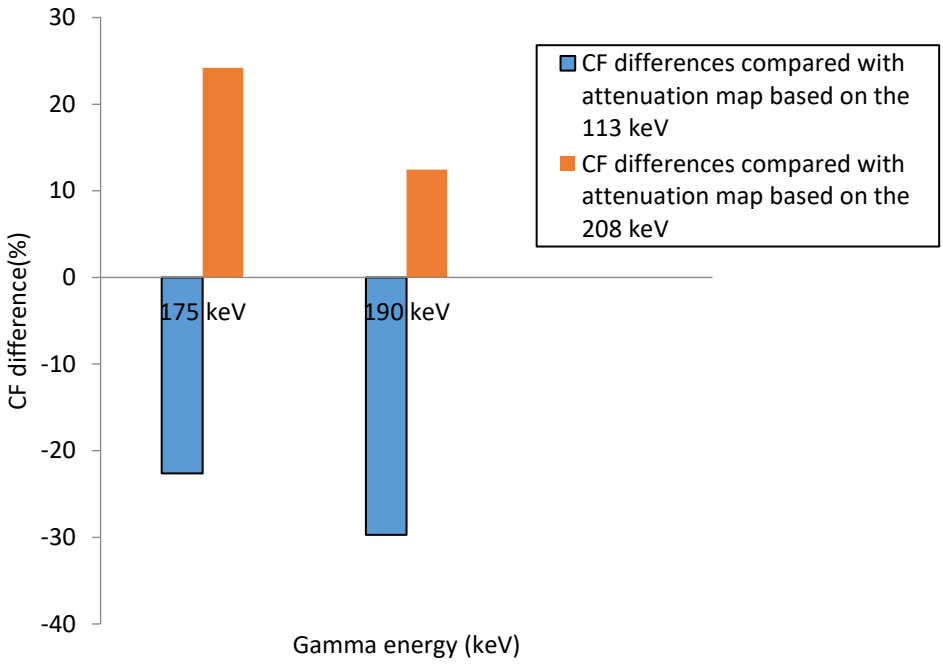

Figure 3.6: The difference in the calculated calibration factors (CFs) using the calculated attenuation map at 175 and 190 keV instead of 113 and 208 keV.

To obtain an ideal combination of the scatter energy windows in the case of using TEW for scatter correction, various scatter windows were applied to 208 keV and 113 keV ^{177}Lu photopeaks. To investigate the accuracy of the scatter correction, for all scatter energy windows (SW) combinations, the scatter fraction (SCF) was determined

and compared to the actual scatter fraction (ASCF) to analyze the rate of the corrected scattered events. The SCF and CF for each SWs, are shown for each photopeak energy in Table 3.3.

Table 3.3: Simulation with SIMIND Monte Carlo code: scatter fraction (SCF) and calibration factor (CF) for different scatter energy windows (SWs).

Combination	Lower scatter window (keV)	Upper scatter window (keV)	SCF	CF
scatter energy windows for the 113 keV photopeak energy				
1 (clinical setting)	84-100.8	123.2-140	0.29	1.9
2	84-100.8	123.2-175	0.28	2.0
3	74-100.8	123.2-140	0.42	1.7
4	74-100.8	123.2-150	0.39	1.8
5	74-100.8	123.2-170	0.29	2.0
6	54-100.8	123.2-133.2	0.43	1.7
7	54-100.8	123.2-170	0.30	1.8
8	54-100.8	123.2-140	0.43	1.7
9	90.8-100.8	123.2-133.2	0.29	2.0
Actual scatter fraction (ASCF): 0.660 CF reference: 1.37 cps MBq^{-1}				
scatter energy windows for the 208 keV photopeak energy				
1 (clinical setting)	172.2-195	220.48-241.28	0.13	2.0
2	142-195	220.4-271.2	0.13	2.0
3	162-195	220.4-251.4	0.13	2.0
4	190-195	220.48-225.48	0.17	1.9
Actual scatter fraction (ASCF): 0.279 CF reference : 1.87 cps MBq^{-1}				

The calculated ACF for the low and high photopeak energies was 0.660 and 0.279, respectively. For the 113 keV photopeak energy, the scatter fraction (SCF) was obtained 0.290 by applying the scatter energy window width same as the clinical set-up (lower scatter window was set as 84-100.8 keV and upper scatter window was set as 123.2-140 keV). Among different combinations which were investigated, the closest SCF to the ASCF was obtained as 0.434 by changing the lower scatter energy

window to the 54-100.8 keV and applying the upper scatter energy window's width as same as the clinical setting. Beside, narrower SW for high photopeak energy than the default clinical setting resulted in decreasing uncertainty in calculated CF. The best combination is shown in table 3.4. For comparison, the scatter energy windows for clinical settings are also included.

Table 3.4: Best scatter energy windows for both photopeak energies of ^{177}Lu from simulation results compared to clinical settings.

Simulation	113 keV photopeak	208 keV photopeak
The best combination of scatter windows	MW: 100.8–123.2 keV (20%) LSW: 54.00–100.8 keV (30%) USW: 123.2–140 keV (13%)	MW: 195–220.4 keV (12%) LSW: 190- 195 keV (1.2%) USW: 220.48- 225.48 keV (1.2%)
Clinical settings	MW: 100.8-123.2 keV (20%) LSW: 84-101 keV (20%) USW: 123-140 keV (13%)	MW: 195-220.48 keV (12%) LSW: 172.2-195 keV (12.4%) USW: 220.48-241.28 keV (9%)

MW: main window, LSW: lower scatter window; USW: upper scatter window.
The values in brackets represent the percentage of the energy window regarding the centered energy.

Moreover, in this work the influence of collimator detector response compensation on the calibration factor determination was investigated. For this purpose, first, the CF for both gamma photopeak energies of ^{177}Lu was calculated by applying the clinical setting for scatter energy windows, AC using attenuation map at 190 keV, and CDR compensation function. Then in the absence of CDR correction, CF was calculated for 113 and 208 keV photopeak energy (Figure 3.7).

For the high gamma photopeak energy the calibration factor was calculated as 2.02 and 2.77 cps MBq^{-1} with or without the CDR correction. Also, for the low gamma photopeak energy, by including the collimator detector response correction, the CF was obtained as 1.95 cps MBq^{-1}, and by excluding the CDR correction, it was 2.21 cps MBq^{-1}. As shown in Figure 3.7, the CDR compensation made 13 and 37%

inaccuracy in estimating the CF for low and high gamma photopeak energies, correspondingly.

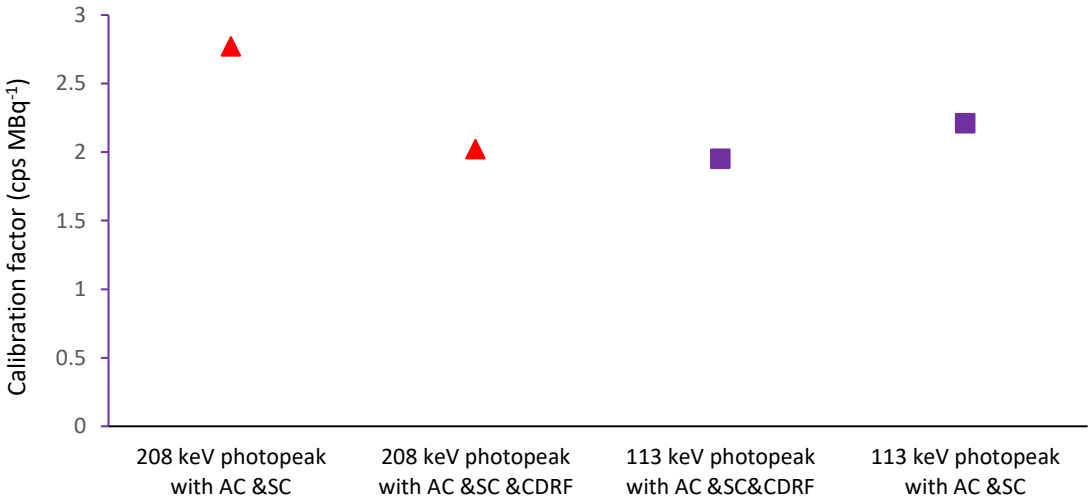

Figure 3.7: Influence of CDR correction on calculation of the calibration factor

3.3 Patient study

The activity uptakes of ^{177}Lu-PSMA I&T for both kidneys and liver were measured for a cohort of six patients who were suffering from prostate cancer, by using the SPECT images and the calculated mCF from the large VOIs. Additionally, by using planar data, activity uptakes in kidneys and liver for each patient were obtained by drawing regions of interest (ROIs) on the ^{177}Lu-PSMA whole-body images at the same indicated time points for SPECT imaging. To determine the time-integrated activity, for both SPECT and planar imaging, the time activity curves of target regions (liver and kidney) were fitted to exponential functions of the first or second order using OLINDA/EXM software. Then, the organ time activity curves (TAC) from planar and SPECT imaging were compared for each patient.

3.3 Patient study

For instance, the time activity curves for liver and a kidney at 5 time points for patient No.1 who had metastases in liver and a high uptake in spleen are shown in Figure 3.8. The activity uptakes of liver and kidney were higher by using the whole-body planar images than the SPECT images. In Figure 3.9, the time activity curves of the liver and kidney are shown for patient No.6 who had no metastases in liver and no uptake in spleen. As there was no SPECT scanning record after 24 hours from the first scanning, the TAC was created based on the data at 4 time points (2, 48, 72, and 168 hours). As it is shown, the kinetic behavior of the liver or a kidney using SPECT images is close to the planar results. In APPENDIX A, the results of two other patients (No 2, and No 5) are given.

After creating the TACs, the personalized absorbed doses to the kidneys and liver from the SPECT data sets were calculated by using OLINDA/EXM software and were compared with planar imaging results. As described in section 2.3.1, all the patients had received the activity in the range of 6470 - 7172 MBq at the first cycles of their therapies. The mean administrated activity of ^{177}Lu-PSMA I&T was 6.9±0.3 GBq. For each patient, by using a series of CT images of PET/CT, the kidney and liver's volumes were obtained in the range of 134-218 ml and 1321-2373 ml, respectively (as mentioned in table 2.7).

As shown in Figure 3.10. the absorbed dose to a kidney using SPECT/CT and planar data is ranged from 0.42 Gy GBq^{-1} to 0.88 Gy GBq^{-1} and from 0.388 Gy GBq^{-1} to 0.92 Gy GBq^{-1}, respectively. The average kidney dose based on planar images was 23% higher than the dose calculated from SPECT/CT data (0.69±0.24 Gy GBq^{-1} vs 0.53±0.21 Gy GBq^{-1}). The average of absorbed dose to the liver using SPECT/CT and planar data was about 0.074±0.019 and 0.097±0.05 Gy GBq^{-1}, respectively. In short, by using the SPECT data sets the mean calculated absorbed doses were smaller than using the planar images. Both for a kidney or the liver, the average absorbed doses using SPECT images was about 23% lower than using planar images.

3.3 Patient study

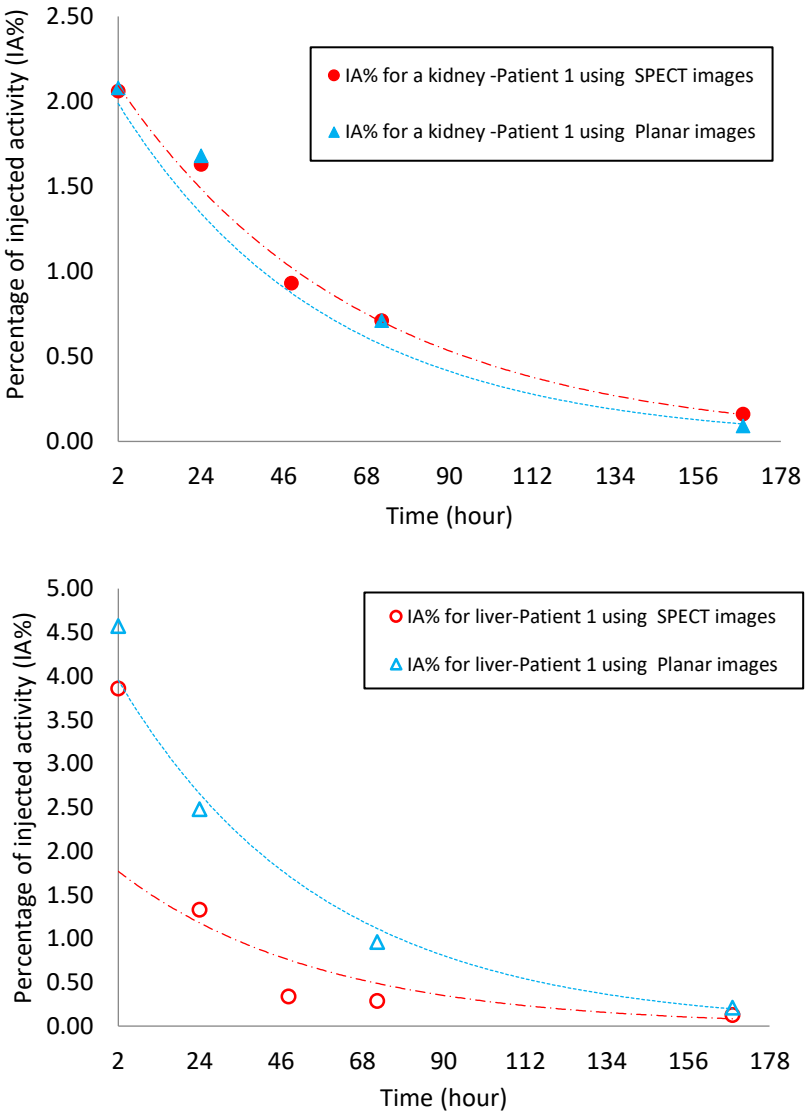

Figure 3.8: Percentage of injected activity (IA%) in a kidney and liver using SPECT and planar images for patient No 1.

3.3 Patient study

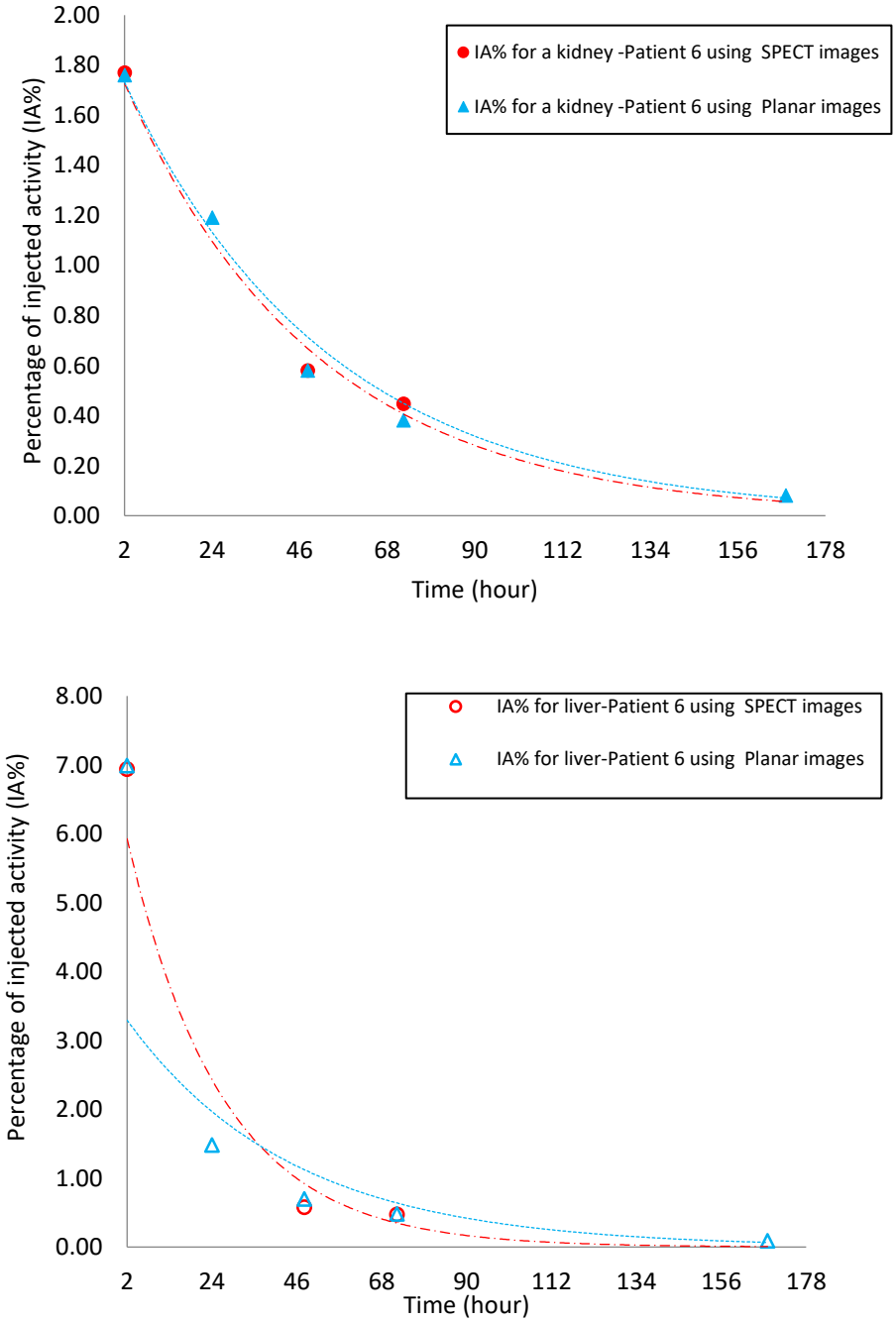

Figure 3.9: Percentage of injected activity (IA%) in kidneys and liver using SPECT and planar images for patient No 6.

3.3 Patient study

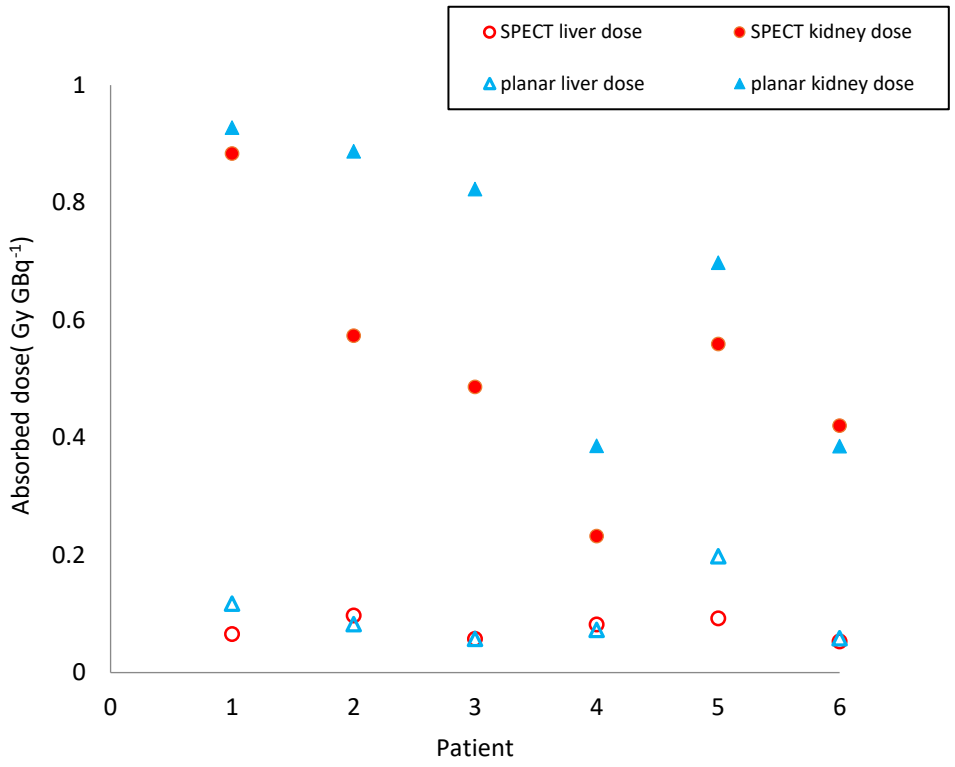

Figure 3.10. Absorbed doses to a kidney and liver for 6 patients derived from SPECT and planar images separately.

4 Discussion

4.1 Calibration factor calculated by the phantom measurements

The purpose of this section is to define the parameters which affect the SPECT calibration factor in order to quantitatively measure an organ activity of ^{177}Lu-PSMA for an individual dosimetry. In this work we applied the mean value of CF of two different volumes of the vials based on the small and large VOIs. The results of activity quantification indicate that it is reasonable to use large or small VOI when applying both photopeak energy windows.

In the current work, for the 208 keV photopeak energy of ^{177}Lu, the average value of the calculated CFs from all experimental measurements using large and small VOIs was 1.4 and 1.25 times larger than for the 113 keV, respectively.

The results of the phantom measurements showed that different activity concentrations using the same volume of the vials, with or without background, do not affect the CF calculation (Figure 3.1 and 3.2). However, there is a significant difference in the calculated CF_L and CF_S, using the same activity concentration for objects with different volumes. It was observed that for the vial with 180 ml volume, the CF_L and CF_S considering both photopeak energies contribution was 46 and 30% higher than the small vial. This difference confirms that using the small VOIs reduces the partial volume effect significantly for the large object. Moreover, it can be concluded that the calculation of the calibration factor in order to calculate activity, using SPECT/CT images, depends on the volume of the object during a phantom measurement.

The variation of the measured activity from the calibrated activity implied that using the mCF_L can cause an underestimation for a lesion or an overestimation for a kidney in dose calculation (refer to Table 3.1). Dewaraja et al. [15] outlined an underestimation in measured activities on a voxel level for small objects. Using the

small VOI in the mCF_S will reduce the uncertainty in activity quantification and may be appropriate in patient studies, when organ volumes are known and homogenous activity distribution in the organ can be assumed.

In the presence of a background activity the deviation of the measured activity for the 180 ml vial of a known activity was only 3% higher than the difference in the absence of the background (Table 3:1: E and G). For this reason, it can be concluded that during the activity calculation of an organ the effect of the activity uptake by neighbor organs can be neglected. The analysis of the measured background activity in the phantom body, using $mCF_{L,}$ showed the effect of the ununiformed activity distribution (hot spot) as an underestimation in the measurements. However, using the small VOI the influence of the ununiformed distribution of the ^{177}Lu on the activity estimation was decreased. As the activity uptake of a lesion or organ like a kidney or liver may be non-uniform, using the small VOI is a robust approach to calculate the activity more accurately.

4.2 Analyzing the simulation results

The simulation showed that in quantitative SPECT/CT imaging the attenuation map, scatter correction and the width of the SWs have a considerable effect on the accuracy of the calculated CF which consequently results in an over/underestimation of the measured activity. It was found that generating an individual attenuation map at each of the main gamma photopeak energies of ^{177}Lu may reduce inaccuracy in CF and hence, in activity quantification. Furthermore, we found that a suitable scatter energy window width decreases the inaccuracy of the CF calculation. However, the ESSE technique may be a better alternative for scatter correction.

Before applying any reconstruction on projected images, contribution of various detected photons as the image components was studied. The events in collimator were subdivided in different categories for both gamma photopeak energies of ^{177}Lu. It was observed that for 113 keV gamma photopeak, only the two events from geometrical

collimated primary attenuated photons and geometrical collimated from scattered photons from the phantom, with/out backscattering, are detected in collimator. Frey et al. [35] concluded, for low energy incident photons, the effect of the scattering in the crystal is small. However, for the 208 keV the contribution of the scattered photons was considerable in comparison with the low gamma photopeak energy of ^{177}Lu. The results confirmed this fact that at higher energies the scattering in crystal and behind the crystal becomes important. In addition, the image quality and consequently the quantification accuracy are affected by septal penetration.

In addition, as explained in section 2.2, to quantify the calibration factors, a reference calibration factor (considering all detected photons excluding scattered events) by applying AC at 190 keV was calculated. This factor was about 15% lower than the CF_L calculated by the phantom measurement in water using the 25 ml vial (Figure 3.5). This difference may be related to differences in geometry and effective energy window. The calculated CF_L by applying the TEW correction including both photopeak energies was only 5% higher than CF_L calculated by the phantom measurements in water (Figure 3.5). Considering the study of Sandström et al. [25], quantification problems in SPECT imaging mostly is related to AC and SC. For example, although AC is included in the SPECT reconstruction software, they showed the inevitable inaccuracy in the order of 10% due to it. D'Arienzo et al. [27] analyzed four different reference conditions for gamma camera calibration. They showed by using a well-calibrated field instrument that there is an uncertainty about 5% for gamma camera calibration factor.

The attenuation correction showed a considerable dependency to the gamma energy on which AM was created (Figure 3.6). The simulation results showed an under/over estimation in CF calculation by generation the AM at 190 and 175 keV for low and high photopeak energy, correspondingly. The calculated CF for the 113 and 208 keV peak was about 7% and 12% smaller by applying the attenuation map generated at 190

keV, compared to the attenuation map at 175 keV (^{177}Lu weighted energy). These differences are in the line with the recommendation in MIRD pamphlet No. 26 [4]. It may be established that the implemented AM at 190 keV (which is a default clinical setting) in experimental measurement reduces the accuracy of CF calculation.

In the section 2.1.2, the different SWs in the recent quantitative phantom studies are listed in Table 2.4. Robinson et al. showed in their phantom measurements that for activities higher than 200 MBq of ^{177}Lu, the width of SW of ±3% for the both photopeak energies can be sufficient for the scatter correction. However, they showed an uncertainty in dose calculation by applying TEW correction on SPECT images. In the current work, it was observed that the clinical setting causes -56.1% and -54.8% inaccuracy in the scattered photon estimation, for the 113 and 208 keV, respectively. The results showed that for the 113 keV photopeak the inaccuracy will be reduced to -34% if the width of the LSW is about 3 times wider than the clinical setting. The simulation results confirmed the sufficiency of the USW width which is used in clinical applications. It may be concluded that the LSW for low photopeak energy was broader than the USW due to the high background of scatter photons below the 113 keV which should be excluded from the detected photons. However, because of the down-scattered photons, the USW for low photopeak energy should not be wider than the MW width. It was observed that using the abutting windows with same width does not improve the scattered photons estimation and caused more inaccuracy in CF calculation. Therefore, it is concluded that the noise sensitivity of the LSW and USW is not the same. The ideal SW width for the 208 keV photopeak was obtained by a smaller LSW and USW compared to the clinical setting (about 5 and 4 times smaller, respectively). The width of the SW for high photopeak energy influences the scatter contribution less than the SW of the lower photopeak; this is compatible with the findings of Delker et al. [14] and Uribe et al. [28] who considered the high photopeak energy of ^{177}Lu in their studies. De Nijs et al. [24] concluded that TEW is noise

sensitive and a broader energy make this method much more stable for dynamic studies; however, the results of the current work confirm this only for LSW of the 113 keV peak. Although, the noise sensitivity seemed to be negligible for the higher gamma photopeak energy in the current work, narrower SW at 208 keV can reduce biased estimate of scatter in MW, and hence reduces the uncertainty in scattered photons estimation. By using the suggested combination of the SW in this work, the scatter fractions (SCF) were close to the mentioned range in the MIRD pamphlet 26 [4]. Moreover, these values were closer to the related actual scatter fraction (ASCF) than using other SW combinations (Table 3.3). Hence, the results confirmed the better scatter correction by using the optimal combination. This showed that if TEW is applied a better scatter correction can be achieved by adapting suitable SW widths, especially for low photopeak energy.

In table 4.1, the difference of the calculated CF using different SC methods and SW energy combinations from the CF reference is summarized. Using ESSE as the scatter correction method resulted in a calibration factor closer to the CF reference value than using the TEW correction method. Therefore, it can be concluded that applying the TEW correction may not exclude the scatter events perfectly compared to the ESSE method and results in an inaccuracy around 23% in quantitative activity measurements. This reconfirms the results from de Nijs et al. [24]. They showed that for quantitative ^{177}Lu imaging both photopeak energies can be utilized when the ESSE correction technique is applied. In their work, the difference between the calculated and the real activity was less than 10%. However, as is shown in table 4.1, using the ideal SWs, the difference was reduced to 9%.

The effect of collimator detector response compensation was studied for both photopeak energies of ^{177}Lu. The results showed that, by excluding the CDR correction during an image reconstruction, there will be an overestimation in CF calculation. However, the influence of this correction was much more noticeable for higher gamma

photopeak energy than the lower one (Figure 3.7). Considering the impact of collimator detector response compensation, it is concluded that OSEM with CDR allowed an equivalent or better SPECT image quality compared to the OSEM without CDR.

Table 4. 1: Difference of calculated CF using TEW and ESSE as scatters correction methods, and scatter energy windows from the CF reference value.

Difference of the calculated CF from the CF reference (%)	
Scatter correction method	
ESSE	+6
Scatter energy windows	
Optimal combination	+9
Clinical settings (TEW)	+23

Overall, the simulation results showed that in quantitative SPECT/CT imaging the attenuation map, the scatter correction, the width of the scatter energy windows, and the collimator detector response have considerable effects on the accuracy of the calculated CF which consequently results in over/underestimation of the measured activity. It was found that the ESSE method is a good alternative for scatter correction. In addition, as the TEW method is a widely accepted technique in clinical practice, better SC can be achieved by adapting suitable SW widths, especially for the low photopeak energy, and consequently a better activity uptake in vivo dosimetry can be calculated.

4.3 Analyzing the measured activities and doses from patient data

Since the β particles from ^{177}Lu travel maximum 2 mm within the patient body and the pixel (voxel) size of SPECT image in this work was about 4.79 mm, it can be concluded that all energy is absorbed in each voxel locally. The comparison between planar and SPECT results, displayed approximately a similar kinetic behavior of the

activity disposal for a kidney. For the first five patients who had metastases in liver and higher uptake of the ^{177}Lu-labeled PSMA I&T in spleen, in both organs, there was about 30% of difference between the data of SPECT and planar images, but for patient 6 who had no metastases in the liver and no high uptake in the spleen; obviously, the differences between the SPECT and planar results was smaller than 10%. In this limited patient cohort, the difference in dose values based on planar or SPECT/CT data was less than the inter-individual variation. Overall, the mean absorbed doses to the liver and a kidney, using SPECT quantitative data were smaller than the planar results. The results of this work are comparable to the results of Delker et al. [14] and Okamoto et al. [7] by considering the differences in the amounts of the mean injected activity and imaging methods (Table 4.2). The difference between the mean calculated doses reported by Okamoto et al. [7] by using planar images and our work using SPECT images is because of the differences in imaging methods. Although there is no certainty which method causes more accurate dose calculation, the mean absorbed doses to the liver and kidney using SPECT images in this work were 20 and 11% smaller than the mean calculated doses for the corresponding organ found by Delker et al. [14] using similar imaging technique. As reported by Sandström et al. [25], and Larsson et al. [17], there is an independency between the administrated activity and the behavior of the kidney activity uptake. Hence, regardless of the difference between the mean administrated activity in this work and the mean injected activities reported by Delker et al. [14], the absorbed dose in the kidney was approximately in the same range. Larsson et al. [17] calculated the absorbed dose for kidney in the range of 0.38-1.7 Gy GBq^{-1} by administrating an activity in the range of 3.3-8.4 GBq. On the other hand, Sandström et al. [25] by applying similar activity of ^{177}Lu-DOTA(0), 7.4 GBq, for a cohort of 24 patients, measured the absorbed dose for kidney and liver. Their results showed a considerable variation between the quantities of kidneys' dose for 24 patients. The mean absorbed dose was as 7.23±4.6 Gy. Moreover, Sandström et al.

4.3 Analyzing the measured activities and doses from patient data

[25] compared the calculated doses using SPECT and planar images, and reported an overestimation in calculated doses using planar images due to the overlapping of organs' boundaries. Therefore, the differences between the calculated doses reported by Okamoto et al. [7] using planar images and the results of our work using SPECT images originate from different imaging methods that have been used. Also note that using SPECT/CT data in the case of metastases diseases or high activity uptake in spleen and colon can avoid dose overestimation for critical organs like kidney and liver. In other words, an abdominal imaging using SPECT/CT can be acceptable in clinical practice for the purpose of absorbed dose estimation. Although, as the kinetics of the radionuclide varies within one patient to another and is related to the history of patients' diseases, it is not easy to conclude which imaging method is better to use. Moreover, regarding the results of phantom and simulation measurements, implementing a suitable scatter energy windows and scatter correction method may result in more accurate absorbed dose estimation.

Table 4.2: Comparison of the absorbed doses to normal organs in Gy GBq^{-1} between this work and two recent publications [7, 14].

	Delker et al. (2016) using SPECT images	Okamoto et al. (2017) using planar images	This work using SPECT images	This work using Planar images
Mean activity (GBq ± SD)	3.6±0.1	7.3±0.32	6.9±0.3	6.9±0.3
Kidney (mean dose ± SD)	0.6±0.21	0.71±0.25	0.53±0.21	0.69±0.24
Liver (mean dose ±SD)	0.1±0.06	0.12±0.07	0.08±0.02	0.1±0.05
Number of the patients	5	15	6	6

SD: standard deviation

Conclusion and future work

To improve quantitative ^{177}Lu SPECT imaging, findings of this work showed that the geometrical parameters of a vial, e.g. the size and shape should be considered during the calibration process. In this work it was observed that using a small volume of interest (VOIs) within an object reduces the partial volume effect. This reduction of partial volume effect improved accuracy of the calculated calibration factor. Moreover, it was observed that calculated CF varies for each photopeak energy due to various intrinsic detector and collimator sensitivities. The results indicate that the use of both photopeak energy windows for quantitative ^{177}Lu imaging is a reliable approach.

Simulation results of current work indicate that unwanted events, such as attenuation and scattering, cause image quality degradation, and thus appropriate corrections are needed to improve SPECT image quality. The findings demonstrate a considerable influence of the attenuation map, scatter correction method and scatter window width on the SPECT/CT calibration process. Using various attenuation maps, the CF primarily varies because of missed attenuated photons. Moreover, the difference in the calculated CF values using the effective scatter source estimation (ESSE) and the triple energy window (TEW) methods in the simulation is caused by the scattering of the photons in water which represents the patient´s body. As the TEW method is a widely accepted technique in clinical practice, it was found that using a broader width for the lower SW of the 113 keV photopeak energy compared to the clinical setting improves the scatter correction and accuracy of the activity calculation. Although scatter estimation for the higher photopeak energy is less affected by scatter window width than for the lower photopeak energy, a narrower SW can improve the calculated CF. Moreover, our results suggest that using ESSE as a scatter correction method leads to a more accurate activity estimation compared to TEW method hence decreases

uncertainty in the organ absorbed dose calculation. Overall, the result from phantom and simulation measurements indicate that complete count recovery can be improved by applying the ESSE scatter correction method or utilizing the proposed combination of scatter energy windows if TEW is applied.

Furthermore, in the limited patient cohort in this work, the difference in calculated dose values based on planar or SPECT/CT data was less than the inter-individual variation. Besides the variation of the calibration factor, the main differences compared to dosimetry based on planar imaging are caused by overlapping in colon, spleen, and metastases. Hence, an accurate organ delineation for dose calculation is required if planar images are used. Finally, we demonstrated the feasibility of calibrating SPECT/CT patient data for the purpose of dose calculation.

Future Work

In this work, it was demonstrated that the width of energy window for the lower SW of the 113 keV photopeak energy can improve the scatter correction, and therefore the accuracy of the activity calculation. Since the TEW method is a common technique in clinical purposes in Klinikum Rechts der Isar, the suggested energy windows setting based on the numerical results of this work is suggested to be implemented in quantitative ^{177}Lu SPECT imaging in order to be verified experimentally. Furthermore, as the ESSE method has not been evaluated by phantoms or clinical measurements, it is suggested to incorporate this method into 177Lu-PSMA I&T SPECT imaging to verify the simulation results in patient dosimetry.

Overall, further evaluations should be focused on optimizing imaging and reconstruction parameters towards a clinically feasible SPECT/CT protocol covering the whole-body.

As the quality of the CT images from SPECT/CT is not as good as the CT images from PET/CT, we suggest to perform co-registration between these two different series of

images. There are various medical image processing and analyzing software which have the registration module like NiftyReg, 3D Slicer, Elastix, and SYNGO. However, these software are designed and developed to register the images with same modality e.g. MRI-MRI or two different modalities e.g. CT-MRI or MRI-PET. Hence, it is suggested to investigate the image registration method between CT images from SPECT/CT and CT images from PET/CT. Since an accurate definition of the region of interests can achieve a more realistic estimation of absorbed dose, further research must be undertaken to enhance the fusion of co-registered CT images and SPECT images. It proposes to calculate the absorbed dose by using the SPECT/CT images before and after co-registration to evaluate whether co-registered images can be used in absolute dosimetry or not.

Appendix A

In this appendix the percentage of injected activity (IA %) in a kidney and liver using SPECT and planar images for patient No 2 and No 3 are shown.

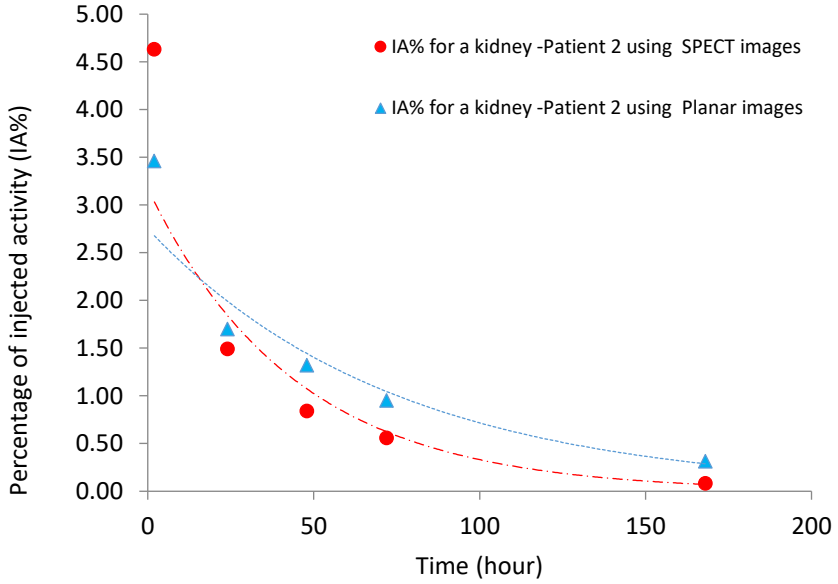

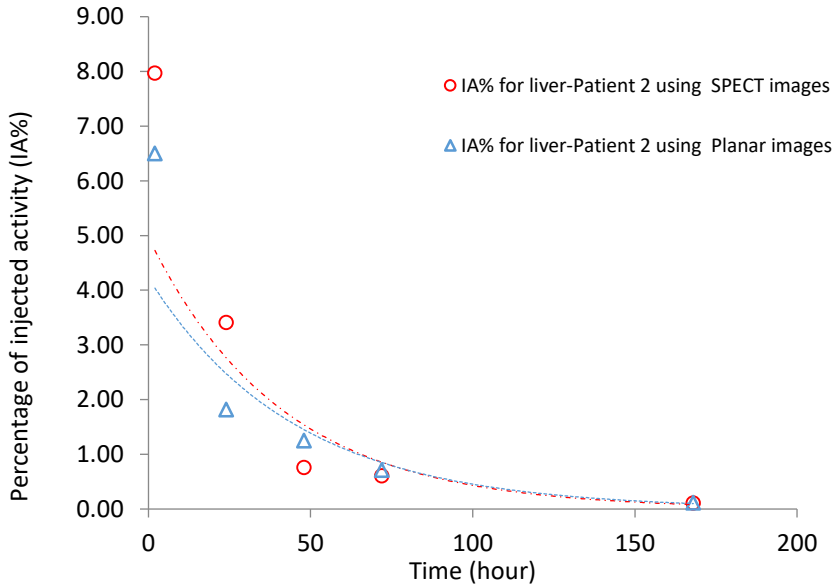

Percentage of injected activity (IA%) in kidneys and liver using SPECT and planar images for patient No 2.

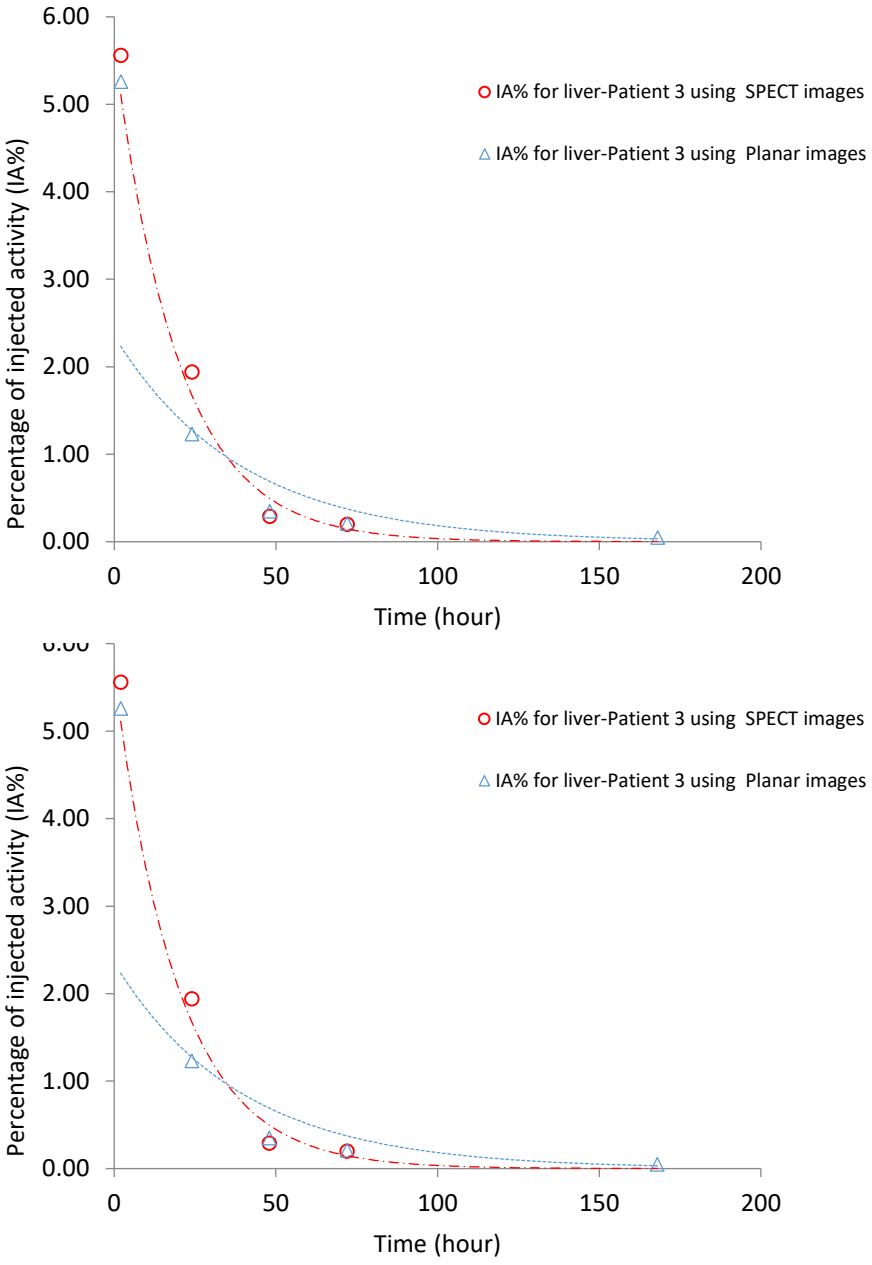

Percentage of injected activity (IA%) in kidneys and liver using SPECT and planar images for patient No 3.

List of abbreviation

SPECT	Single Positron Emission Computed Tomography
PET	Positron Emission Tomography
SC	Scatter Correction
AC	Attenuation Correction
AM	Attenuation Map
CDR	Collimator Detector Response
FOV	Field of View
TEW	Triple Energy window
DEW	Dual Energy Window
ESSE	Effective Source Scatter Estimation
MLEM	Maximum Likelihood Expectation-Maximization
OSEM	Ordered Subsets Expectation Maximization
CF	Calibration Factor
MW	Main Energy Window
LSW	Lower Scatter Energy Window
USW	Upper Scatter Energy Window
TRF	Total Response Function (TRF)
ROI	Region Of Interest

VOI	Volume of Interest
D	Deviation
SF	Scatter Fraction
ASF	Actual Scatter Fraction
TAC	Time ActivityCurve
SW	Scatter Window
FWHM	Full Width at Half Maximum
MRI	Magnetic Resonance Imaging

List of tables

Table 1.1: Common radionuclides used in targeted radiotherapy [3]. 2

Table 2. 1: SPECT acquisition parameters (clinical setting). 30
Table 2.2: SPECT reconstruction parameters (clinical settings). 31
Table 2.3: Configuration of the phantom measurements and ^{177}Lu activities inside the vials used for the calibration factor calculation. 33
Table 2.4: Energy window settings used in current and previous works 35
Table 2. 5: Different combination of scatter windows which used during TEW modeling... 45
Table 2.6: Frequently used parameters by SIMIND for generating CDRF table. 47
Table 2.7: Data set of six patients. 49

Table 3.1 SPECT phantom validation measurements using mean CF based on two different VOIs. 59
Table 3.2: Contribution of gamma photopeak energy of ^{177} Lu in different events in the detector crystal. 62
Table 3.3: Simulation with SIMIND Monte Carlo code: scatter fraction (SCF) and calibration factor (CF) for different scatter energy windows (SWs). 65
Table 3.4: Best scatter energy windows for both photopeak energies of ^{177}Lu from simulation results compared to clinical settings. 66

Table 4. 1: Difference of calculated CF using TEW and ESSE as scatters correction methods, and scatter energy windows from the CF reference value. 77
Table 4.2: Comparison of the absorbed doses to normal organs in Gy GBq^{-1} between this work and two recent publications [7, 14]. 79

List of figures

Figure 1. 1: Schematic of scintillation camera performance..... 13
Figure 1.2: Illustration of projection coordinates corresponding to a parallel-beam scanning geometry for SPECT according to [58]: f(x,y) is radionuclide distribution, and θ is the angle of the projection 15
Figure 1.3: Reconstruction procedure using MLEM and OSEM methods. 16
Figure 1.4: Relation between number of subsets and iterations and their effects on the quality of final image. Each row shows the number of iteration, while each column presents the number of subsets. A) 1 subset B) 4 subsets and C) 16 subsets, according to [61]. 17
Figure 1.5: True activity measurement is possible from an ideal SPECT imaging. The emitted photons from each organ reach the SPECT camera without any attenuation and scattering. 18
Figure 1.6: Distances from the point to the edge of the object are calculated in the Chang compensation method, according to [18] 21
Figure 1.7: Principle of Dual Energy Window (DEW) correction for a given pixel and projection, according to [70]. 23
Figure 1.8: Principle of TEW scatter correction method for a given pixel and projection, according to [17]. 24
Figure 1.9: Schematic of the factors which include in collimator detector response function. 26

Figure 2.1: a) Siemens Symbia T6 SPECT/CT with NEMA IEC body phantom filled with water including a vial with 25 ml volume (calibrated activity of 651 MBq). b) Anterior SPECT image of water filled phantom (green) with background activity of 178.1 MBq including a 180 ml vial with 440 MBq activity. Background activity distribution was non-uniform (hot spot). 32
Figure 2.2: The average volume of kidney was calculated using a number of patient data sets 32
Figure 2.3: Large volume covered the geometrical size of the vial.: a) Top view, b) Lateral view , and c) Front view. 36
Figure 2. 4: A schematic of the phantom, source and camera directions in CHANGE program [72]. 38
Figure 2.5: Full decay spectra of ^{177}Lu were used for simulation to include the principal energy used for imaging and those energies which are important for the component of septal penetration in the projection images. 39

Figure 2.6: Created attenuation map (AM) for attenuation correction. 40
Figure 2.7: The kernel images were created to use for ESSE modeling. 43
Figure 2.8: Magnitude of the Full width at half maximum (FWHM) is depended to the photopeak energy and the source distances from the surface of the collimator. 46
Figure 2.9: Image (point source) became blurred when the distance of the source to the collimator increased. 46
Figure 2.10: ROI for liver and kidney were drawn using planar image: a) anterior and b) posterior view..... 50
Figure 2.11: a) An abdominal CT image used to define organ, b) An abdominal SPECT image used to obtain total counts within organ, and c) SPECT/CT image fusion..... 51
Figure 2.12: Left graphs show time-activity curves (TAC); right screen shows the activity of each organ at 4 different measured time. The imported data into the table was created using the function described in eq. 2.13. 53

Figure 3.1: The calculated calibration factor using large VOIs for each photopeak energy window with various activity concentrations of ^{177}Lu-PSMA I&T in a 25 ml vial (filled symbols) and a 180 ml vial (open symbols) representing a lesion and a kidney, respectively. 56
Figure 3.2: The calculated calibration factor using small VOIs for each photopeak energy window with various activity concentrations of ^{177}Lu-PSMA I&T in a 25 ml vial (filled symbol) and a 180 ml vial (open symbol) representing a lesion and a kidney respectively. . 58
Figure 3.3: Simulated cylinder phantom including a 25 ml vial with 650 MBq of ^{177}Lu in water. 60
Figure 3.4: Contribution of various events with collimator and phantom medium: a) low photopeak energy (113 keV) and b) high photopeak energy (208 keV). 63
Figure 3.5: Different scatter correction (SC) methods: the triple energy window (TEW) and effective scatter source estimation (ESSE) during simulation in water and air, compared to experimental measurements. The collimator detector response (CDR) and attenuation correction (AC) were implemented in all simulations. 63
Figure 3.6: The difference in the calculated calibration factors (CFs) using the calculated attenuation map at 175 and 190 keV instead of 113 and 208 keV..... 64
Figure 3.7: Influence of CDR correction on calculation of the calibration factor 67
Figure 3.8: Percentage of injected activity (IA%) in a kidney and liver using SPECT and planar images for patient No 1. 69
Figure 3.9: Percentage of injected activity (IA%) in kidneys and liver using SPECT and planar images for patient No 6. 70

Figure 3.10. Absorbed doses to a kidney and liver for 6 patients derived from SPECT and planar images separately. 71

Bibliography

1. Bray F, Ferlay J, Soerjomataram I, Siegel RL, Torre LA, Jemal A. Global cancer statistics 2018: GLOBOCAN estimates of incidence and mortality worldwide for 36 cancers in 185 countries. CA Cancer J Clin. 2018;68:394-424.

2. Jadvar H. Targeted Radionuclide Therapy: An Evolution Toward Precision Cancer Treatment. 2017 Agu;209 (2):277-88.

3. Emmett LA-Ohoo, Willowson K, Violet J, Shin J, Blanksby A, Lee J. Lutetium (177) PSMA radionuclide therapy for men with prostate cancer: a review of the current literature and discussion of practical aspects of therapy. J Med Radiat Sci. 2017:52-60.

4. Ljungberg M, Celler A, Konijnenberg MW, Eckerman KF, Dewaraja YK, Sjogreen-Gleisner K, Bolch WE, Brill AB, Fahey F, Fisher DR, Hobbs R, Howell RW, Meredith RF, Sgouros G, Zanzonico P, Bacher K, Chiesa C, Flux G, Lassmann M, Strigari L, Walrand S. MIRD Pamphlet No. 26: Joint EANM/MIRD Guidelines for Quantitative 177Lu SPECT Applied for Dosimetry of Radiopharmaceutical Therapy. Journal of nuclear medicine : official publication, Society of Nuclear Medicine. 2016;57:151-62. doi:10.2967/jnumed.115.159012.

5. Jiang L, Miao Z, Liu H, Ren G, Bao A, Cutler CS, Shi H, Cheng Z. 177Lu-labeled RGD-BBN heterodimeric peptide for targeting prostate carcinoma. Nuclear medicine communications. 2013;34:909-14. doi:10.1097/MNM.0b013e328362d2b6.

6. Lantry LE, Cappelletti E, Maddalena ME, Fox JS, Feng W, Chen J, Thomas R, Eaton SM, Bogdan NJ, Arunachalam T, Reubi JC, Raju N, Metcalfe EC, Lattuada L, Linder KE, Swenson RE, Tweedle MF, Nunn AD. 177Lu-AMBA: Synthesis and characterization of a selective 177Lu-labeled GRP-R agonist for systemic radiotherapy of prostate cancer. Journal of nuclear medicine : official publication, Society of Nuclear Medicine. 2006;47:1144-52.

7. Okamoto S, Thieme A, Allmann J, D'Alessandria C, Maurer T, Retz M, Tauber R, Heck MM, Wester HJ, Tamaki N, Fendler WP, Herrmann K, Pfob CH, Scheidhauer K, Schwaiger M, Ziegler S, Eiber M. Radiation dosimetry for 177Lu-PSMA I&T in metastatic castration-resistant prostate cancer: Absorbed dose in normal organs and tumor lesions. Journal of nuclear medicine : official publication, Society of Nuclear Medicine. 2017;58:445-50. doi:10.2967/jnumed.116.178483.

8. Ahmadzadehfar H, Essler M, Schafers M, Rahbar K. Radioligand therapy with 177Lu-PSMA-617 of metastatic prostate cancer has already been arrived in clinical use. Nuclear medicine and biology. 2016;43:835. doi:10.1016/j.nucmedbio.2016.08.003.

9. Ahmadzadehfar H, Eppard E, Kurpig S, Fimmers R, Yordanova A, Schlenkhoff CD, Gartner F, Rogenhofer S, Essler M. Therapeutic response and side effects of repeated radioligand therapy with 177Lu-PSMA-DKFZ-617 of castrate-resistant metastatic prostate cancer. Oncotarget. 2016;7:12477-88. doi:10.18632/oncotarget.7245.

10. Rahbar K, Schmidt M, Heinzel A, Eppard E, Bode A, Yordanova A, Claesener M, Ahmadzadehfar H. Response and Tolerability of a Single Dose of 177Lu-PSMA-617 in

Patients with Metastatic Castration-Resistant Prostate Cancer: A Multicenter Retrospective Analysis. Journal of nuclear medicine : official publication, Society of Nuclear Medicine. 2016;57:1334-8. doi:10.2967/jnumed.116.173757.

11. Kratochwil C, Giesel FL, Eder M, Afshar-Oromieh A, Benesova M, Mier W, Kopka K, Haberkorn U. [(1)(7)(7)Lu]Lutetium-labelled PSMA ligand-induced remission in a patient with metastatic prostate cancer. European journal of nuclear medicine and molecular imaging. 2015;42:987-8. doi:10.1007/s00259-014-2978-1.

12. Fendler WP, Reinhardt S, Ilhan H, Delker A, Boning G, Gildehaus FJ, Stief C, Bartenstein P, Gratzke C, Lehner S, Rominger A. Preliminary experience with dosimetry, response and patient reported outcome after 177Lu-PSMA-617 therapy for metastatic castration-resistant prostate cancer. Oncotarget. 2017;8:3581-90. doi:10.18632/oncotarget.12240.

13. Baum RP, Kulkarni HR, Schuchardt C, Singh A, Wirtz M, Wiessalla S, Schottelius M, Mueller D, Klette I, Wester HJ. 177Lu-Labeled Prostate-Specific Membrane Antigen Radioligand Therapy of Metastatic Castration-Resistant Prostate Cancer: Safety and Efficacy. Journal of nuclear medicine : official publication, Society of Nuclear Medicine. 2016;57:1006-13. doi:10.2967/jnumed.115.168443.

14. Delker A, Fendler WP, Kratochwil C, Brunegraf A, Gosewisch A, Gildehaus FJ, Tritschler S, Stief CG, Kopka K, Haberkorn U, Bartenstein P, Boning G. Dosimetry for ^{177}Lu-DKFZ-PSMA-617: a new radiopharmaceutical for the treatment of metastatic prostate cancer. European journal of nuclear medicine and molecular imaging. 2016;43:42-51. doi:10.1007/s00259-015-3174-7.

15. Dewaraja YK, Frey EC, Sgouros G, Brill AB, Roberson P, Zanzonico PB, Ljungberg M. MIRD Pamphlet No. 23: Quantitative SPECT for Patient-Specific 3-Dimensional Dosimetry in Internal Radionuclide Therapy. Journal of nuclear medicine : official publication, Society of Nuclear Medicine. 2012;53:1310-25. doi:10.2967/jnumed.111.100123.

16. Bailey DL, Hennessy TM, Willowson KP, Henry EC, Chan DL, Aslani A, Roach PJ. In vivo quantification of ^{177}Lu with planar whole-body and SPECT/CT gamma camera imaging. EJNMMI physics. 2015;2:20. doi:10.1186/s40658-015-0123-2.

17. Larsson M, Bernhardt P, Svensson JB, Wangberg B, Ahlman H, Forssell-Aronsson E. Estimation of absorbed dose to the kidneys in patients after treatment with 177Lu-octreotate: comparison between methods based on planar scintigraphy. EJNMMI research. 2012;2:49. doi:10.1186/2191-219x-2-49.

18. IAEA. Quantitative Nuclear Medicine Imaging: Concepts, Requirements and Methods, Human Health Reports No.9. Vienna: INTERNATIONAL ATOMIC ENERGY AGENCY; 2014.

19. Podgoršak EB. Absolute Radiation Dosimetry. In: Podgorsak EB, editor. Radiation Physics for Medical Physicists. Cham: Springer International Publishing; 2016. p. 671-758.

20. Zimmerman BE, Grosev D, Buvat I, Coca Perez MA, Frey EC, Green A, Krisanachinda A, Lassmann M, Ljungberg M, Pozzo L, Quadir KA, Teran Gretter MA, Van Staden J, Poli GL. Multi-centre evaluation of accuracy and reproducibility of planar and SPECT image quantification: An IAEA phantom study. Zeitschrift fur medizinische Physik. 2017;27:98-112. doi:10.1016/j.zemedi.2016.03.008.

21. Sanders JC, Kuwert T, Hornegger J, Ritt P. Quantitative SPECT/CT imaging of (177)Lu with in vivo validation in patients undergoing peptide receptor radionuclide therapy. Molecular imaging and biology : MIB : the official publication of the Academy of Molecular Imaging. 2015;17:585-93. doi:10.1007/s11307-014-0806-4.

22. Willowson K, Bailey DL, Baldock C. Quantitative SPECT reconstruction using CT-derived corrections. Physics in medicine and biology. 2008;53:3099-112. doi:10.1088/0031-9155/53/12/002.

23. Gustafsson J, Brolin G, Cox M, Ljungberg M, Johansson L, Sjögreen Gleisner K. Uncertainty propagation for SPECT/CT-based renal dosimetry in ^{177}Lu peptide receptor radionuclide therapy. Phys Med Biol. 2015;60:8329.

24. de Nijs R, Lagerburg V, Klausen TL, Holm S. Improving quantitative dosimetry in (177)Lu-DOTATATE SPECT by energy window-based scatter corrections. Nuclear medicine communications. 2014;35:522-33. doi:10.1097/MNM.0000000000000079.

25. Sandström M, Garske U, Granberg D, Sundin A, Lundqvist H. Individualized dosimetry in patients undergoing therapy with ^{177}Lu-DOTA-D-Phe1-Tyr3-octreotate. EJNMMI physics. 2010;37:212-25. doi:10.1007/s00259-009-1216-8.

26. Hippeläinen E, Tenhunen M, Mäenpää H, Sohlberg A. Quantitative accuracy of ^{177}Lu SPECT reconstruction using different compensation methods: phantom and patient studies. EJNMMI research. 2016;6:16. doi:10.1186/s13550-016-0172-0.

27. D'Arienzo M, Cazzato M, Cozzella ML, Cox M, D'Andrea M, Fazio A, Fenwick A, Iaccarino G, Johansson L, Strigari L, Ungania S, De Felice P. Gamma camera calibration and validation for quantitative SPECT imaging with ^{177}Lu. Applied radiation and isotopes : including data, instrumentation and methods for use in agriculture, industry and medicine. 2016;112:156-64. doi:10.1016/j.apradiso.2016.03.007.

28. Uribe CF, Esquinas PL, Tanguay J, Gonzalez M, Gaudin E, Beauregard J-M, Celler A. Accuracy of ^{177}Lu activity quantification in SPECT imaging: a phantom study. EJNMMI physics. 2017;4:2. doi:10.1186/s40658-016-0170-3.

29. Zhao W, Esquinas PL, Hou X, Uribe CF, Gonzalez M, Beauregard J-M, Dewaraja YK, Celler A. Determination of gamma camera calibration factors for quantitation of therapeutic radioisotopes. EJNMMI physics. 2018;5:8. doi:10.1186/s40658-018-0208-9.

30. Grassi E, Fioroni F, Ferri V, Mezzenga E, Sarti MA, Paulus T, Lanconelli N, Filice A, Versari A, Iori M. Quantitative comparison between the commercial software STRATOS® by Philips and a homemade software for voxel-dosimetry in radiopeptide therapy. Physica Medica. 2015;31:72-9. doi:https://doi.org/10.1016/j.ejmp.2014.10.002.

31. Wevrett J, Fenwick A, Scuffham J, Nisbet A. Development of a calibration protocol for quantitative imaging for molecular radiotherapy dosimetry. Radiat Phys Chem. 2017;140:355-60. doi:10.1016/j.radphyschem.2017.02.053.

32. Ljungberg M, Strand SE. A Monte Carlo program for the simulation of scintillation camera characteristics. Computer methods and programs in biomedicine. 1989;29:257-72.

33. He B, Wahl RL, Du Y, Sgouros G, Jacene H, Flinn I, Frey EC. Comparison of residence time estimation methods for radioimmunotherapy dosimetry and treatment planning:Monte Carlo simulation studies. IEEE transactions on medical imaging. 2008;27:521-30. doi:10.1109/tmi.2007.908131.

34. Frey EC, Tsui BMW. A new method for modeling the spatially-variant, object-dependent scatter response function in SPECT. IEEE Nuclear Science Symposium. 1996;2:1082-86. doi:10.1109/NSSMIC.1996.591559.

35. Frey EC, Tsui BMW. Collimator-Detector Response Compensation in SPECT. In: Zaidi H, editor. Quantitative Analysis in Nuclear Medicine Imaging. Boston, MA: Springer US; 2006. p. 141-66.

36. Hudson HM, Larkin RS. Accelerated image reconstruction using ordered subsets of projection data. IEEE transactions on medical imaging. 1994;13:601-9. doi:10.1109/42.363108.

37. Shao L, Freifelder R, Karp JS. Triple energy window scatter correction technique in PET. IEEE transactions on medical imaging. 1994;13:641-8. doi:10.1109/42.363104.

38. Ljunberg M, Strand SE, King MA. Monte Carlo calculation in nuclear medicine. Boca Raton, FL: CRC Press, Taylor & Francis Group; 2013.p. 1-357.

39. Grassi E, Fioroni F, Berenato S, Patterson N, Ferri V, Braglia L, Filice A, Versari A, Iori M, Spezi E. Effect of image registration on 3D absorbed dose calculations in 177Lu-DOTATOC peptide receptor radionuclide therapy. Physica Medica: European Journal of Medical Physics. 2018;45:177-85. doi:10.1016/j.ejmp.2017.11.021.

40. Doherty JO. A review of 3D image-based dosimetry, technical considerations and emerging perspectives in (90)Y microsphere therapy. Journal of diagnostic imaging in therapy. 2015;2:1-34. doi:10.17229/jdit.2015-0428-016.

41. Li T, Ao ECI, Lambert B, Brans B, Vandenberghe S, Mok GSP. Quantitative Imaging for Targeted Radionuclide Therapy Dosimetry - Technical Review. Theranostics. 2017;7:4551-65. doi:10.7150/thno.19782.

42. Roy S, Carass A, Jog A, Prince JL, Lee J. MR to CT Registration of Brains using Image Synthesis. Proc SPIE Int Soc Opt Eng. 2014: 9034. doi:10.1117/12.2043954

43. Johansson A, Garpebring A, Karlsson M, Asklund T, Nyholm T. Improved quality of computed tomography substitute derived from magnetic resonance (MR) data by incorporation of spatial information--potential application for MR-only radiotherapy and attenuation correction in positron emission tomography. Acta Oncol 2013;52:1369-73.

44. Korsager AS, Carl J, Østergaard LR. MR-CT registration using a Ni-Ti prostate stent in image-guided radiotherapy of prostate cancer. Med Phys. 2013;40:061907-1.

45. Lian J, Xing L, Hunjan S, Dumoulin C, Levin J, Lo A, Watkins R, Rohling K, Giaquinto R, Kim D, Spielman D, B. D. Mapping of the prostate in endorectal coil-based MRI/MRSI and CT: a deformable registration and validation study. . Med Phys. 2004;31:3087-94.

46. Novikov RG. An inversion formula for the attenuated X-ray transformation. Archiv für Mathematik. 2002;40:145-67.

47. Morris P, Chua SS-C, Groves A, Rao S, Costa KD, Richens JL, O'Shea P, Hwang M, Oborski M, Laymon C, Imani F, Mountz J, Panchuelo RMS, Stephenson MC, Francis ST, Morris PG, Harris A, Siesky B, Primus S, Zore M, Tobe LA, Acikel V, Atalar E, Botnar RM, Makowski MR, Thote T, Moran S, Willett NJ, Neu CP, Lin A, Guldberg RE, Hoad CL, Francis ST, Gowland PA, Marciani L. Contributor contact details. In: Morris P, editor. Biomedical Imaging: Woodhead Publishing; 2014. p. 1-318.

48. Kalra A. Chapter 9 - Developing FE Human Models From Medical Images. In: Yang K-H, editor. Basic Finite Element Method as Applied to Injury Biomechanics: Academic Press; 2018. p. 389-415.

49. Bibb R, Eggbeer D, Paterson A. 2 - Medical imaging. In: Bibb R, Eggbeer D, Paterson A, editors. Medical Modelling (Second Edition). Oxford: Woodhead Publishing; 2015. p. 7-34.

50. Povoski SP, Neff RL, Mojzisik CM, O'Malley DM, Hinkle GH, Hall NC, Murrey DA, Jr., Knopp MV, Martin EW, Jr. A comprehensive overview of radioguided surgery using gamma detection probe technology. World journal of surgical oncology. 2009;7:11. doi:10.1186/1477-7819-7-11.

51. Sarikaya I, Sarikaya A, Reba RC. Gamma probes and their use in tumor detection in colorectal cancer. International seminars in surgical oncology : ISSO. 2008;5:25. doi:10.1186/1477-7800-5-25.

52. Alazraki N, Glass Ec Fau - Castronovo F, Castronovo F Fau - Olmos RAV, Olmos Ra Fau - Podoloff D, Podoloff D. Procedure guideline for lymphoscintigraphy and the use of intraoperative gamma probe for sentinel lymph node localization in melanoma of intermediate thickness 1.0. Journal of nuclear medicine : official publication, Society of Nuclear Medicine. 2002;43:1414-8.

53. Blahd WH. Ben Cassen and the development of the rectilinear scanner. Semin Nucl Med. 1996;26(3):165-70.

54. Peterson TE, Furenlid LR. SPECT detectors: the Anger Camera and beyond. Phys Med Biol. 2011;56:R145-82. doi:10.1088/0031-9155/56/17/r01.

55. Zhang X, Smith N, Webb A. Chapter one - Medical imaging. In: Feng DD, editor. Biomedical Information Technology (Second Edition): Academic Press; 2020. p. 3-49.

56. Ghaly M, Links JM, Frey E. Optimization of energy window and evaluation of scatter compensation methods in myocardial perfusion SPECT using the ideal observer with and without model mismatch and an anthropomorphic model observer. J Med Imaging (Bellingham). 2015;2(1). doi:10.1117/1.JMI.2.1.015502.

57. Patton JA, Turkington TG. SPECT/CT physical principles and attenuation correction. J Nucl Med Technol. 2008;36(1):1-10. doi:10.2967/jnmt.107.046839. Epub 2008 Feb 20.

58. Huang Q, You J, Zeng GL, Gullberg GT. Reconstruction from uniformly attenuated SPECT projection data using the DBH method. IEEE transactions on medical imaging. 2009;28:17-29. doi:10.1109/TMI.2008.923974.

59. Lee T, Cho S. Performance comparison of OS-EM algorithm with ML-EM in Digital Tomosynthesis. World Congress on Medical Physics and Biomedical Engineering. Beijing, China: Springer; 2013. p. 1136-8.

60. Bruyant PP. Analytic and Iterative Reconstruction Algorithms in SPECT. Journal of Nuclear Medicine. 2002;43:1343.

61. Alessio A, Kinahan P. PET image reconstruction. Nuclear medicine. 2006;1:1-22.

62. McKetty MH. The AAPM/RSNA physics tutorial for residents. X-ray attenuation. RadioGraphics. 1998;18:151-63. doi:10.1148/radiographics.18.1.9460114.

63. Rosenthal MS, Cullom J, Hawkins W, Moore SC, Tsui BM, Yester M. Quantitative SPECT imaging: a review and recommendations by the Focus Committee of the Society of Nuclear Medicine Computer and Instrumentation Council. Journal of nuclear medicine : official publication, Society of Nuclear Medicine. 1995;36:1489-513.

64. Pan X, Wong WH, Chen CT, Liu J. Correction for photon attenuation in SPECT: analytical framework, average attenuation factors, and a new hybrid approach. Phys Med Biol. 1993;38:1219-34.

65. Fleming JS. A technique for using CT images in attenuation correction and quantification in SPECT. Nuclear medicine communications. 1989;10:83-97.

66. Bailey DL, Hutton BF, Walker PJ. Improved SPECT using simultaneous emission and transmission tomography. Journal of nuclear medicine : official publication, Society of Nuclear Medicine. 1987;28:844-51.

67. Malko JA, Van Heertum RL, Gullberg GT, Kowalsky WP. SPECT liver imaging using an iterative attenuation correction algorithm and an external flood source. Journal of nuclear medicine : official publication, Society of Nuclear Medicine. 1986;27:701-5.

68. Dorbala S, Ananthasubramaniam K, Armstrong IS, Chareonthaitawee P, DePuey EG, Einstein AJ, Gropler RJ, Holly TA, Mahmarian JJ, Park M-A, Polk DM, Russell R, Slomka PJ, Thompson RC, Wells RG. Single Photon Emission Computed Tomography (SPECT) Myocardial Perfusion Imaging Guidelines: Instrumentation, Acquisition, Processing, and Interpretation. Journal of Nuclear Cardiology. 2018;25:1784-846. doi:10.1007/s12350-018-1283-y.

69. Asl MN, Sadremomtaz A, Bitarafa-Rajabi A. Evaluation of six scatter correction methods based on spectral analysis in (99m)Tc SPECT imaging using SIMIND Monte Carlo simulation. Med Phys. 2013;38:189-97.

70. Koral K, Swailem F, Buchbinder S, Clinthorne N, Rogers W, Tsui B. SPECT Dual-Energy-Window Compton Correction: Scatter Multiplier Required for Quantification. Journal of nuclear medicine : official publication, Society of Nuclear Medicine. 1990;31:90-8.

71. Ogawa K. Simulation study of triple-energy-window scatter correction in combined Tl-201, Tc-99m SPECT. Annals of nuclear medicine. 1994;8:277-81.

72. Rong X, Du Y Fau - Ljungberg M, Ljungberg M Fau - Rault E, Rault E Fau - Vandenberghe S, Vandenberghe S Fau - Frey EC, Frey EC. Development and evaluation of an improved quantitative (90)Y bremsstrahlung SPECT method. Med Phys. 2012;39:2346-58. doi:10.1118/1.3700174.

73. Bolch WE, Eckerman Kf Fau - Sgouros G, Sgouros G Fau - Thomas SR, Thomas SR. MIRD pamphlet No. 21: a generalized schema for radiopharmaceutical dosimetry standardization of nomenclature. J Nucl Med. 2009 Mar;50(3):477-84.

74. Guo L. The applications of SPECT in internal dosimetry. Foreign Medical Sciences Section of Radiation Medicine and Nuclear Medicine. 2004;28:67-70.

75. Halty A, Badel J-N, Kochebina O, Sarrut D. Image-based SPECT calibration based on the evaluation of the Fraction of Activity in the Field of View. EJNMMI physics. 2018;5:11. doi:10.1186/s40658-018-0209-8.

76. Vija AH, Hawman EG, Engdahl JC. Analysis of a SPECT OSEM reconstruction method with 3D beam modeling and optional attenuation correction: phantom studies. 1996 IEEE Nuclear Science Symposium Conference Record. 2003;4:2662-6. doi:10.1109/NSSMIC.2003.1352436.

77. NEMA NEMA. Performance Measurements of Positron Emission Tomographs (PETS). Washington, D.C.; 2001.

78. Robinson AP, Tipping J, Cullen DM, Hamilton D. The influence of triple energy window scatter correction on activity quantification for ^{177}Lu molecular radiotherapy. Phys Med Biol. 2016;61:5107-21.

79. Schulthess GKv. Molecular Anatomic Imaging: PET-CT and SPECT-CT Integrated Modality Imaging. second edition ed. Philadelphia, USA: Lippincott Williams & Wilkins; 2007.

80. Ljungberg M. The SIMIND Monte Carlo Program: http://www.radfys.lu.se/simind 2012.

81. Seo Y, Wong KH, Sun M, Franc B, Hawkins RA, Hasegawa BH. Calculation and validation of the use of effective attenuation coefficient for attenuation correction in In-111 SPECT. Med Phys. 2005;32:3628-35.

82. Lee TC, Alessio AM, Miyaoka RM, Kinahan PE. Morphology supporting function: attenuation correction for SPECT/CT, PET/CT, and PET/MR imaging. Q J Nucl Med Mol Imaging. 2016;60:25-39.

83. Andrew PR, Jill T, David MC, David H. The influence of triple energy window scatter correction on activity quantification for 1 7 7 Lu molecular radiotherapy. Physics in Medicine & Biology. 2016;61:5107.

84. Stabin MG, Sparks Rb Fau - Crowe E, Crowe E. OLINDA/EXM: the second-generation personal computer software for internal dose assessment in nuclear medicine. J Nucl Med 2005 46(6):1023-7.

List of publication

Journal paper

- Karimi Ghodoosi, E., D' Alessandria, C., Li, Y., Bartel, A., Köhner, M., Höllriegl,V., Navab, N., Eiber, M., Li, W.B., Frey, E., Ziegler, S. (2018): The effect of attenuation map, scatter energy window width, and volume of interest on the calibration factor calculation in quantitative ^{177}Lu SPECT imaging: Simulation and phantom study. Physica Medica 56, 74-80

Conference contributions and proceedings

- Karimi Ghodoosi, E., D'Alessandria, C., Eiber, M., Li, W.B., Navab, N., Ziegler, S.: Comparison of absorbed dose to kidneys using quantitative SPECT/CT and whole body planar images for Lu-177-PSMA I&T in prostate cancer therapy. Eur. J. Nucl. Med. Mol. Imaging 45, S112-S113 (2018)

- Karimi Ghodoosi, E., D´Alessandria, C., Li, Y., Ghaly, M., Navab, N., Li, W.B., Frey, E., Ziegler, S. (2017): Evaluating image degradation influence on calibration factor estimation in quantitative Lu-177-PSMA SPECT. ICRP/ERPW Conference, 10.-12. 10.2017, Paris

- Karimi Ghodoosi, E., D´Alessandria, C., Bartel, A., Meisinger, C., Köhner, M., Hoeschen, C., Navab, N., Frisch, B., Eiber, M., Ziegler, S. (2016): Improving quantitative imaging accuracy for the purpose of dosimetry of ^{177}Lu-PSMA I&T used in prostate cancer therapy. DGMP 2016 Conference, 7.-10.9.2016, Würzburg

Acknowledgements

First of all, I would like to thank Prof. Dr. Sibylle Ziegler for her precious supervision, advices, and continuous support. I am grateful, that you gave me the opportunity to follow my own ideas in this project. I am pleased that you supported me to go to Johns Hopkins University as a visiting student and work there. This opportunity brought me a precious experience, and knowledge. Your support motivated me to improve myself. You helped me to progress professionally and personally.

My sincere thanks go to my bright supervisor at Helmholtz Zentrum Muenchen Dr. Wei Bo Li. You were always open to new ideas and provided me very valuable guidance and support.

I would like to express my very great appreciation to my mentor Prof. Dr. Nassir Navab. Your feedback and positive comments definitely helped directing my project towards the right direction.

I am particularly grateful for the assistance given by Dr. Eric Frey and Gary Li at Johns Hopkins University. Your bright advices at the right time improved my knowledge of numerical analyses of reconstructed images using Monte Carlo simulation (SIMIND & Python).

Thanks to the Institute of Radiation Protection at Helmholtz Zentrum: Dr. Nina Petoussi-Henss, Dr. Vera Höllriegl, and Monika Keusch. From colleagues you became friends, and from friends you became my second family. Thank you Prof. Dr. Christoph Hoeschen for giving me the opportunity to come to Germany and work in your group.

My special thanks are extended to Dr. Calogero D'Alessandria, Alexander Bartel, and Markus Köhner from nuclear medicine department of Klinikum rechts der Isar for

providing me all necessary facilities for experimental measurements and patient data study.

Thanks to my family in Iran. Thanks to my parents for your support and trust in all my choices since I was a little kid. I know it has been difficult to be that far away. Thank you for all your emotional support.

Thank you to all my friends who have been part of my non-academic life in Munich. Although I tend to be doing academic work all the time, my time as a PhD student would have been so difficult if I did not have you to make me happy and balance my work. Especial thanks go to Mohammad, Zohreh, Mahmout, Nazereh, Negar, and Fatemeh.